Master's Thesis

A STUDY ON PRELIMINARY DESIGN OF MULTI-STABLE 4D PRINTING PART USING NONLINEAR FINITE ELEMENT ANALYSIS

Eunseo Lee

Department of Mechanical Engineering

Graduate School of UNIST

2019

A STUDY ON PRELIMINARY DESIGN OF MULTI-STABLE 4D PRINTING PART USING NONLINEAR FINITE ELEMENT ANALYSIS

Eunseo Lee

Department of Mechanical Engineering

Graduate School of UNIST

A Study on Preliminary Design of Multi-stable 4D Printing Part using Nonlinear Finite Element Analysis

A thesis
submitted to the Graduate School of UNIST
in partial fulfillment of the
requirements for the degree of
Master of Science

Eunseo Lee

12/14/2018

Approved by

Namhun Kim

Advisor
Namhun Kim

A Study on Preliminary Design of Multi-stable 4D Printing Part using Nonlinear Finite Element Analysis

Eunseo Lee

This certifies that the thesis of Eunseo Lee is approved.

12/14/2018

Namhun Kim

Advisor: Namhun Kim

Young Chul Jun

Sang Hoon Kang

Abstract

4D printing is a method of 3D printing in which the printed part reacts to stimuli and transforms into another intended shape over time. Much research on 4D printing has been done recently, but most cases relate only to the shrinkage or expansion of the smart material used to manufacture the part. This thesis focuses on the structure of the part itself and how it can move from one stable position into another, adopting a multi-stable structure to 4D printing. The multi-stable structure has two or more stable states in which the entire piece stays at rest with no external force. When not in one, it shows a tendency to return to the stable state. This property enables the design of a 4D printed part that shifts quickly and accurately into an intended shape. The design of the multi-stable 4D printed part is a combination of various parameters. However, the dynamic behavior of the 4D printed part with multi-stability is difficult to predict using an analytical method due to the high nonlinearity in the material properties and the geometry. Furthermore, it is not efficient regarding cost and time to go through a trial-and-error experiment in order to investigate the influences of each variable on the part.

In this thesis, a finite element (FE) simulation method is introduced to efficiently predict the effects of the various parameters on the behavior of bi-stable rotatable structures and their strain energy via the commercial tool ABAQUS. The simulated structures consist of an inner rotational part, a fixed outer ring, and four beams connecting them. Several assumptions were made on the FE model to increase the convergence of the simulations and reduce the computation time. From the results of the FE simulations, the shape of beam deflection and the strain energy are observed to determine the bi-stability and the position of stable states. In addition, a statistical analysis is carried out to determine the effects of a variable on the strain energy.

Subsequently, the process of designing a 4D rotational model based on the simulation results of the rotatable structures was presented. The new 4D rotational model has stability at two points under room temperature. If the temperature gets high after the inner rotational part is rotated to the second stable state, the model is restored to the original shape. For this newly designed model, the feasibility of performing the intended function was analyzed through the FE simulation. Finally, the results were compared with the motion of the printed model to validate it.

This study describes the FE modeling skills required to reduce convergence failure in simulations of the multi-stable structure. In addition, I verified that the use of FE simulation in the design of multi-stable 4D printing part is reliable by showing that the FE results are in good agreement with experimental results in their rotational motion in response to the thermal stimulus. The designed 4D rotational model does not need extra energy consumption to maintain the stable state or to rotate in response to ambient stimuli, so it can work as an active mechanical switch.

Contents

List of Figures

List of Tables

1. Introduction

1.1 Background

Since its invention in the 1980s, 3D printing technology has advanced dramatically and has been used in various field, such as aerospace, automobile, medical, and fashion [1]. 3D printing, also called additive manufacturing, is a generic term for manufacturing parts by stacking materials in a layer-by-layer manner. Unlike conventional processes that subtract materials or use casting, 3D printing technology has the capability to produce complex shaped parts using multiple materials, without additional assembling processes. Along with these strengths, 3D printing technology has recently attracted attention as one of the most essential technologies of the fourth industrial revolution. Lots of countries and corporations are seeing this potential and are investing in the development of new materials, new binding processes, and computer-aided design (CAD) technology [1].

In particular, the application of newly invented materials and the development of accurate, multi-material 3D printing technologies has created the field of 4D printing. 4D printing a type of the 3D printing, to which the dimension of time is added [2]. 4D printed parts respond to external stimulus and change their shape after they are printed. The materials used in 4D printing are usually called smart materials [3]. They have physical properties that vary depending on the surrounding environment, such as temperature, humidity, or light. As stimuli are applied, the physical properties changes, leading the 4D printing part to undergo a predictable shape change. It enables various functions such as self-assembly, self-adaptability, and self-repair [4].

Conventionally, in order to design a system that responds to a stimulus, sensors and actuators are required. To manufacture them, a plurality of parts should be separately manufactured and combined. In contrast, using 4D printing, a part can have its functions without complex assembling processes, as joint or bonded sites can be printed in a single printing process. Using this strength, many researchers have demonstrated the high potential of 4D printing in many areas, such as biomedicine, soft robotics, and adaptive meta-material [5-7]. Also, it is considered as a promising future technology in the fields of architecture and tissue engineering [8, 9].

1.2 Research objective and direction

In much of the research about 4D printing, the techniques for implementing the motion of a 4D printed part have relied on the phenomenon by which the smart material contracts or expands in response to the stimuli [4]. However, since the physical properties of smart materials that can be used in 3D printing may not be constant depending on the printing condition, the shape of printed parts, and the external environment, it is often difficult to accurately predict the dynamic behavior of 4D printed parts. Besides, some of the smart materials used for 4D printing are still in the development stage, so the mechanical properties have not yet reached the level of application. Accordingly, there are some cases of 4D printing that shows the responses to the stimuli take too long, or movements in the models do not reach the intended level [6, 10, 11].

A method of applying multi-stable structure to 4D printing has been suggested as one of the solutions to these problems [12]. Multi-stable structures have two or more stable states in which the entire piece stays at rest with no external force, like a light switch. In order to make transitions between stable states, the energy of a system should exceed the energy barrier between them. If a system successfully reaches this energy barrier, it shifts quickly to the next stable state. Otherwise, it returns to the previous stable state. Using a multi-stable structure is an effective way to implement a fast and accurate shape-shifting motion in a 4D printed part with multiple target positions. Therefore, the model can be usefully applied as an active mechanical switch.

4D printed parts with multi-stability can be designed with a wide variety of geometries and materials. However, it is not easy to analytically predict the behavior and energy under various combinations of possible variables, because a multi-stable 4D printed structure usually includes high nonlinearity in both the motion of the geometry and the properties of the material in a changing ambient environment [13, 14]. It is also costly and time-consuming work to manufacture and test all the parts with different parameters to design an optimal multi-stable 4D printed structure.

To solve this problem, finite element (FE) simulation was used to analyze the mechanical behavior of the models by computer calculation. The main objective of this study is as followings:

- To suggest methods of FE simulation modeling for multi-stable, rotatable structures with nonlinear motion, as well as method for improving the convergence of the simulation.
- To predict the behavior and the strain energy of rotatable models depending on variables in temperature, model geometry and material properties using FE simulation
- To design a 4D rotational model that changes multi-stability depending on temperature,

based on the FE simulation results of rotatable models.

- To analyze the dynamic behavior and the strain energy of the 4D rotational model using FE simulation.

A commercial tool ABAQUS (Simulia, Providence, RI, USA) will be used in the FE simulation. Among the result of the simulation, the shapes of beam deflections and characteristic features in strain energy curves will be discussed, in order to investigate the trends according to the parameters in temperature, geometry, and material properties. Several assumptions in constraints, loads, and simulation steps are used to improve convergence and reduce computation time. The design of the original model and the material property measurements used in this study were provided by the laboratory of Nanophotonics & Metamaterials, UNIST.

1.3 Outline

This thesis consists of five chapters in total. A brief description of the background and the purpose of this thesis are already presented in Chapter 1. In Chapter 2, the related literatures and the background theories will be introduced. Chapter 3 describes the FE model setup for rotatable models with four different beam connection types and then provides an analysis of the results. In Chapter 4, the design of a multi-stable 4D printed model which uses the results from Chapter 3 and the FE simulation of the newly designed model are presented. Chapter 5 presents the conclusions and describes future work.

2. Research background

2.1 4D printing process

The fundamental elements of 4D printing are 3D printing facility, stimulus, stimulus-responsive material, interaction mechanism, and mathematical modeling [4]. These elements enable the targeted and predictable evolution of structures over time. Figure 2.1 shows a categorized summary of the 4D printing process, which is discussed in further detail below.

2.1.1 Printing process

The fabrication of 4D printing part should be backed up by high-tech 3D printing technology. Generally, it requires the capability to print multiple materials simultaneously and to accurately adjust the composition or proportion of the materials. Mainly used 3D printing processes for 4D printing include stereolithography (SLA), direct writing (DW), selective laser melting (SLM), and the PolyJet process [4, 15].

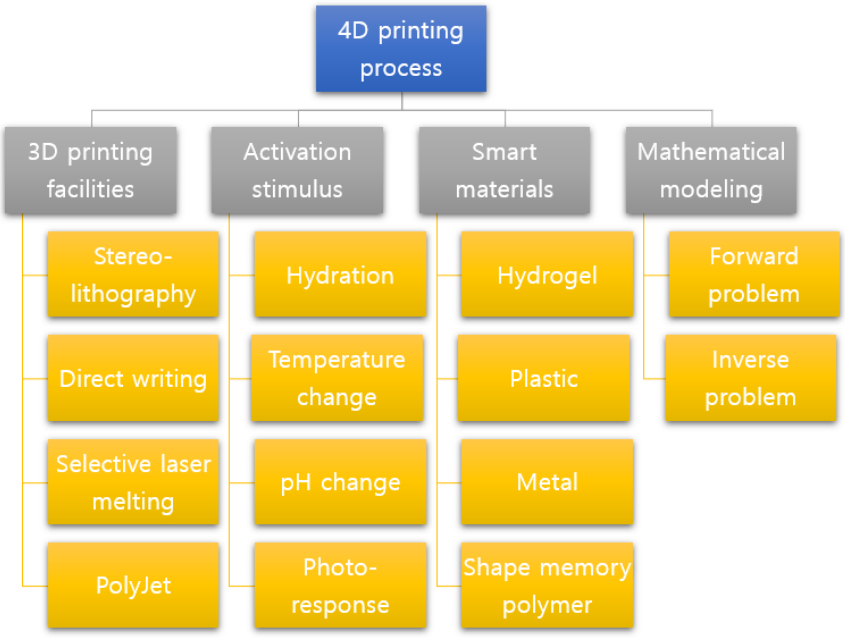

Figure 2.1 The categories of 4D printing process [4].

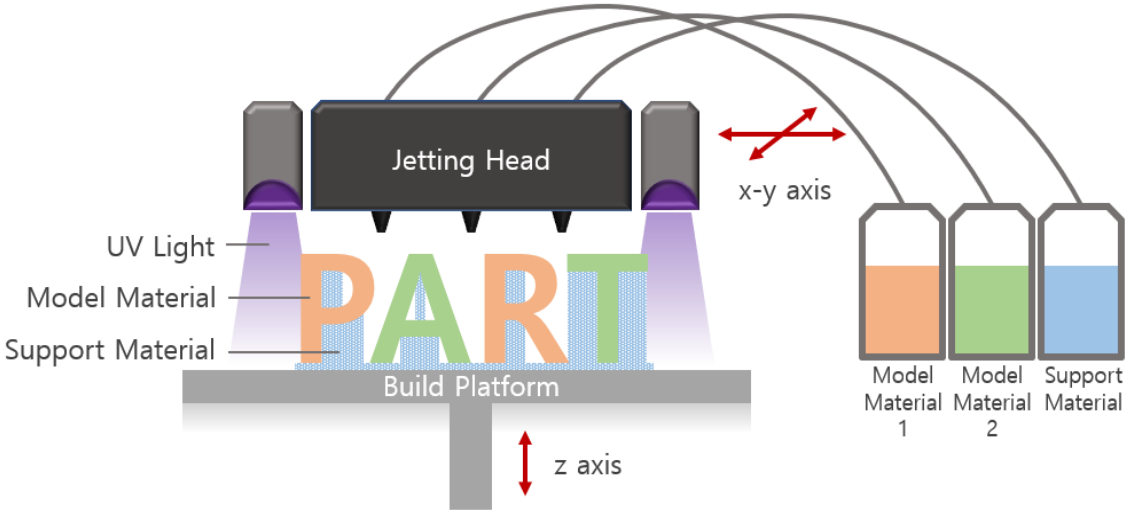

Figure 2.2 The schematic of PolyJet process.

PolyJet printing

PolyJet™ printing is the most appropriate printing process for fabricating multiple materials in a single part, as well as one of the most accurate 3D printing technologies [16]. The PolyJet process is a type of material jetting (MJ) process, which works in a similar way to inkjet printer. Instead of jetting drops of ink onto a paper, PolyJet 3D printers use fine printhead nozzles to deposit droplets of photocurable liquid material onto a build tray in layers as fine as 16 microns to form detailed 3D parts. The material is simultaneously cured via UV light as it is deposited. PolyJet printer uses multiple heads and nozzles to print a variety of materials in a single part [17]. The schematic of PolyJet printer is shown in Figure 2.2.

Parts printed by PolyJet require support structures to build overhanging features and holes. Without support structures, the material can escape its intended form resulting in inaccurate walls, features, and other details. The PolyJet support material is a separate composition formulated to release from the part when jetted off or dissolved with water [18].

Digital Material

The method of combining materials in a PolyJet printer can be represented as digital material. Digital material differs from conventional analog materials, as it is derived from the digital communication language [19]. Like analog signals, analog materials are composed of continuous materials. However, like digital signals consisting of a combination of 0 and 1, digital material

consists of micro-sized three-dimensional space units called physical voxels. Each physical voxel contains only one material, but collections of voxels have various properties, such as different colors, levels of hardness, and transparency. They are accomplished by arranging physical voxels, each containing a different material, either adjacent or in specific patterns [11, 19].

Digital material can have various configurations, as illustrated in Figure 2.3. It can be composed of only one material, or two or more materials may be uniformly arranged by mixing them at a constant ratio in microstructures, thereby macroscopically combining the properties of the materials. It is possible as well to gradually change the material properties of the model by changing the proportion of material arrangement continuously in a particular direction. Also, by arranging the materials in a uniform pattern, the part may have a specific function [4].

2.1.2 Activation stimuli and smart materials

Activation stimuli are required for 4D printed parts to self-evolve. These stimuli and corresponding changes in the parts are closely related to the printing materials and their arrangement. Smart materials used for 4D printing have properties that change according to specific stimuli. In order to use these properties to transform a part into the desired shape, researchers have often used special patterns of materials or specific shapes [7, 20, 21]. Particularly, in some cases [20, 22], they have used a partial deformation on hinges or joints where materials are arranged in patterns. For the remaining parts, they used relatively rigid materials to produce the desired final shape. (Figure 2.4)

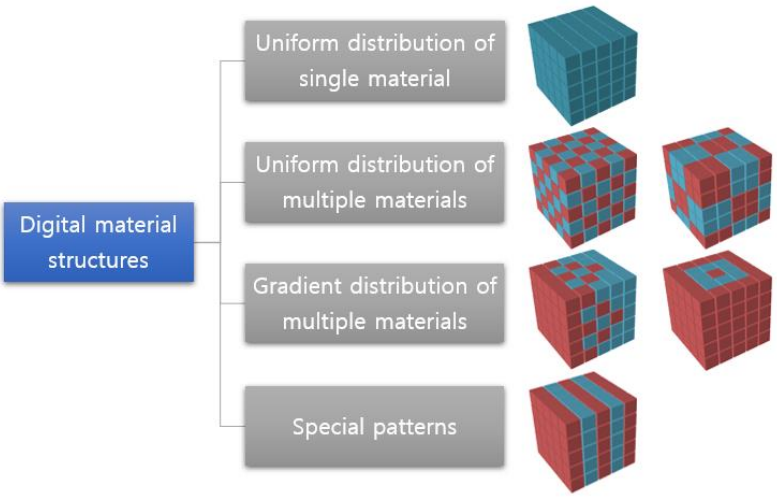

Figure 2.3 Examples of digital material structures [4].

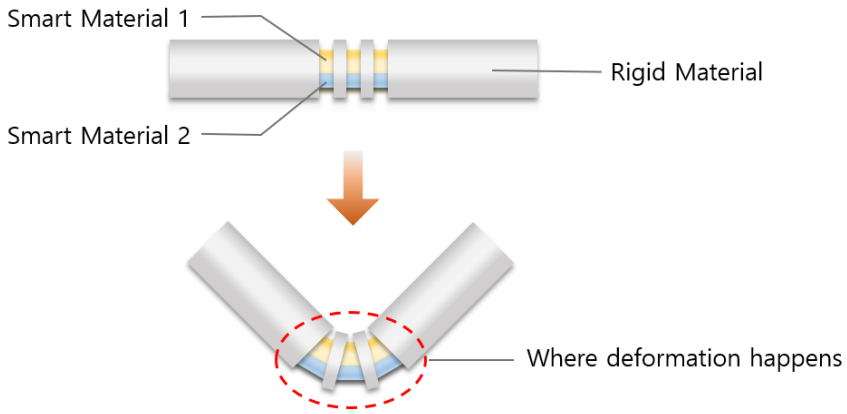

Figure 2.4 Illustration of partial deformation on a joint (Tibbits et al. [20]).

Various stimuli are used to activate a 4D printed part [15], as shown in Figure 2.5. In hydro-mechanics, a dry part is immersed in water to induce deformation, using materials that expand by absorbing water [21]. Also, changes in humidity can cause deformation in smart material [23]. In photo-mechanics, the part is made using a material that stretches or contracts in response to receiving light of a specific wavelength [24]. In thermo-mechanics, various temperature-dependent properties, such as thermal expansion, elastic modulus, and the shape memory effect, induces shape-shifting effects [25]. In what remains of this section, I concentrate on the thermo-mechanics.

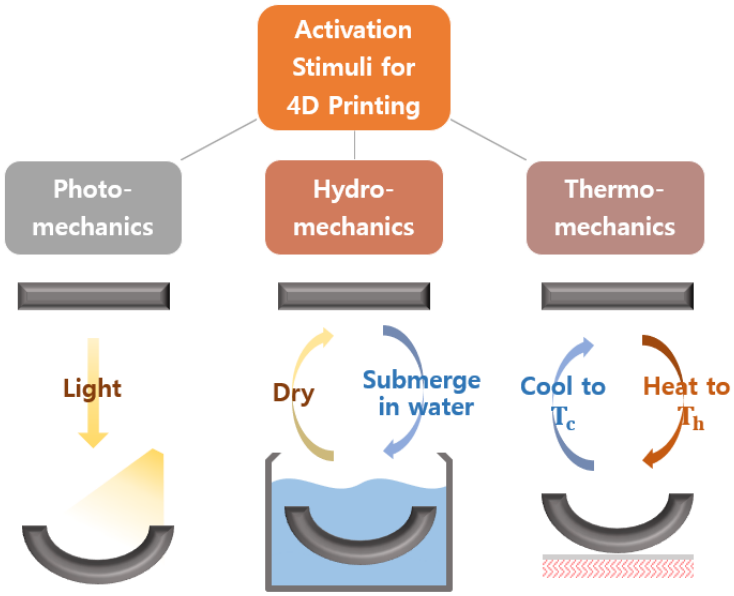

Figure 2.5 Illustration of activation stimuli for 4D printing [15].

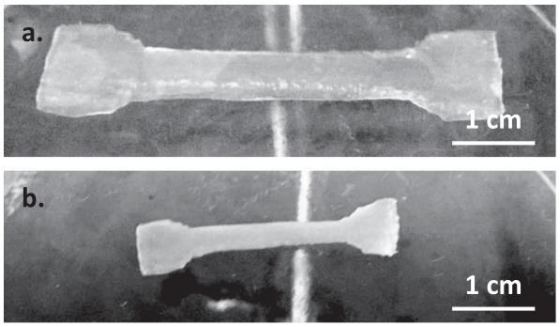

Figure 2.6 Shape shifting of part made by hydrogel (Bakarich et al. [26]).

Shape-shifting in 4D printing part by thermo-mechanics implements deformation using thermal-dependent properties when the temperature changes from low (T_c) to high (T_h) or vice versa. Water is mostly used as a medium to deliver heat from T_h to T_c since it enables heat to be evenly distributed throughout the part [26]. There are various kinds of materials used for thermo-mechanics, including hydrogels, UV hardening plastic and shape memory polymer (SMP) [20, 26, 27].

Hydrogel has been used in 3D printing for more than 20 years because of its suitability in a variety of fields, including tissue engineering [26]. Some hydrogels have significant volume changes depending on environmental changes. Using this characteristic, Bakarich et al. [26] demonstrated the expansion and contraction behavior of a part made with hydrogel (Figure 2.6). This shape-shifting behavior is enabled by linear swing or shrinkage of the thermo-responsive hydrogel in the cold or hot water. However, most hydrogels have a low modulus of ~kPa to ~100kPa [3, 26] and have a solvent diffusion based slow response rate in the time scale of a few tens if minutes, hours, and even days [3, 10, 11]. Therefore, it is difficult to use hydrogels in applications requiring high rigidity or rapid actuation.

In comparison, plastics have relatively high modulus values. Especially, TangoBlack™ and VeroWhite™, which can be printed on PolyJet printers, are materials that has been used in several studies [14, 25, 28], and they can be printed with various properties by mixing them in specific ratio. TangoBlack is in a rubbery state at room temperature polymerized by monomers containing urethane acrylate oligomer, exo-1,7,7-trimethylbicyclo hept-2-yl acrylate, methacrylate oligomer, polyurethane resin, and photo-initiators. VeroWhite is a rigid plastic at room temperature and can be polymerized by an ink consisting of isobornyl acrylate, acrylic monomer, urethane acrylate, epoxy acrylate, acrylic monomer, acrylic oligomer, and photo initiator [29]. Also, a sacrificial material is used for the fabrication of complicated geometries. A hydrophilic gel known as Sup705 polymerized by poly(oxy 1,2-ethanediyl), α-(1-oxo-2-propenyl)-ω-hydroxy-, 1,2-propylene glycol, polyethylene glycol, glycerin, phosphine oxide, phenylbis(2,4,6-trimethylbenzoyl)-, and acrylic

acid ester is used [14]. It is removed using a compressed water jet in a post-processing stage.

The advantage of TangoBlack and VeroWhite is their shape memory ability. In other words, even if the part is transformed into another shape, it can return to its initially printed form when placed in the same environment as the one in which it was originally manufactured. Shape memory polymers (SMPs), activated by a thermal stimulus, are relatively rigid under the glass transition temperature (T_g) but are softened when heat is applied and the temperature exceeds T_g. Using these characteristics, parts made with SMPs generally have two forms: the permanent form and temporary form. The following is the shape-shifting mechanism of SMPs. First, a part in a permanent form is heated to T_h, which is a temperature higher than T_g. Second, it is transformed into a temporary form at T_h. Third, while maintaining the external load, the temperature is lowered to T_c, which is a temperature lower than T_g. Then, the part retains the temporary shape even if the external load is removed. Finally, when the heat is applied until the part reaches T_h, the part returns to the permanent form [30]. The mechanism is illustrated in Figure 2.7.

Using this shape memory behavior, Ge et al. [28] showed several shape changes of active composite laminates using TangoBlack as the elastomeric matrix with T_g~-5℃ and VeroWhite (Gray 60) as the fiber with T_g~47℃. They set T_c=15℃ and T_h=60℃ so that at T_h, both the matrix and fibers are softened, and at T_c, only the matrix is softened, and fibers remain stiff. Various deformed shapes resulted from the same original shape, by differing the fiber architecture, as shown in Figure 2.8 (a).

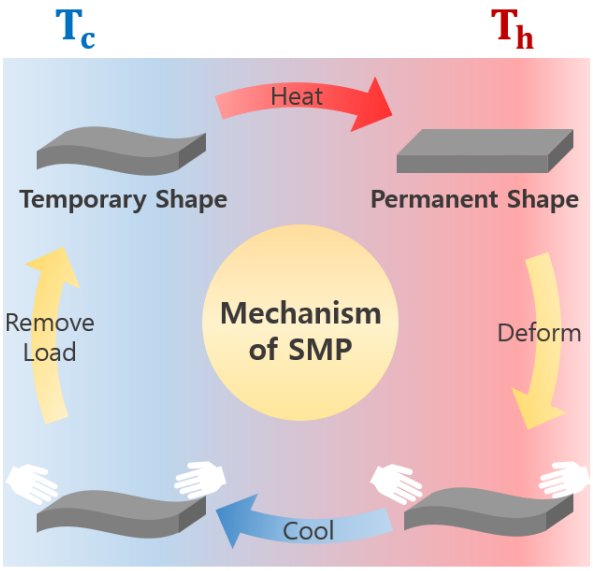

Figure 2.7 Illustration of mechanism of shape memory polymer.

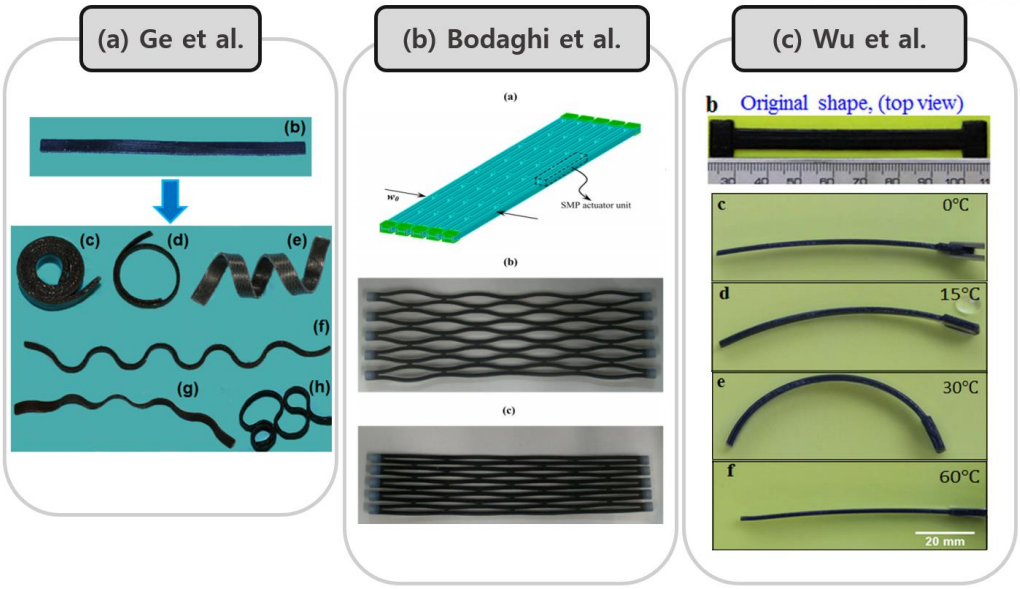

Figure 2.8 (a) The various shape-shifting behavior of active composite laminates (Ge et al. [28]).
(b) The self-expandable/shrinkage structure (Bodaghi et al. [14]).
(c) Multi-shape memory effect of an active composite strip (Wu et al. [25]).

Bodaghi et al. [14] made a self-expandable / shrinkable structure made of SMP meta-material lattice, using TangoBlackPlus™ and VeroWhitePlus™, which are similar materials to those used by Ge et al. [28], and arranged in a fiber and matrix structure. When the structure was heated, the lattice first significantly expanded in the transverse direction and transformed into a new configuration, as shown in Figure 2.8 (b). As time passed, the meta-material lattice got warmer, and it transformed back to its initial state.

Similarly, Wu et al. [25] used TangoBlackPlus and VeroWhite. However, their composite contained two types of fibers to show the multi-shape memory effect of an active composite strip. They used DM8530 (fiber 1) with T_g~57°C and DM9895 (fiber 2) with T_g~38°C. These two fibers have shape memory effects in the temperature range between ~20 °C and ~70°C. As they release the stretched strip at T_c, it was fixed in the first temporary shape. Then they increase temperature of the part to a temperature that is higher than the T_g of the matrix but lower than those of the fibers so that the sample changed into a second temporary shape. When they heated the sample to a temperature higher than the T_gs of both fibers, it recovered the permanent shape (Figure 2.8 (c)).

2.1.3 Mathematical modeling

An appropriate theoretical model for 4D printing consists of four major components [4]. The first is the final desired shape, which may include a desired bending angle, twisting angle, length, or volume. The next is the material structure, such as the volume fractions of fibers and the matrix filament size, orientation, inter-filament spacing, and anisotropy. Equivalently the material structure can be described by the size, shape and spatial arrangement of the voxels. From the perspective of the printing process, the material structure depends on the print paths and nozzle sizes. Material properties make up the third component, and they include shear modulus, Young's modulus, and the interactive properties associated with the stimulus, such as the glass transition temperature and swelling ratio. The final component is the relevant property of the stimulus, such as the temperature and light intensity.

Gladman et al.[3] divided the mathematical modeling method for 4D printing into two categories: the forward problem and the inverse problem. The forward problem is the process of calculating the final desired shape from a set of parameters in material structures, material properties, and stimulus properties. Researches on 4D printing related to the forward problems are mainly fundamental study in order to discover concepts, theories, and relationships. In contrary, the inverse problem starts with the final desired shape, material properties, and stimulus properties then calculates the material structure, the print paths, or the nozzle sizes, as presented in Figure 2.9. Researches related to the inverse problem are application-oriented, meaning that they focus on achieving a desired function or shape.

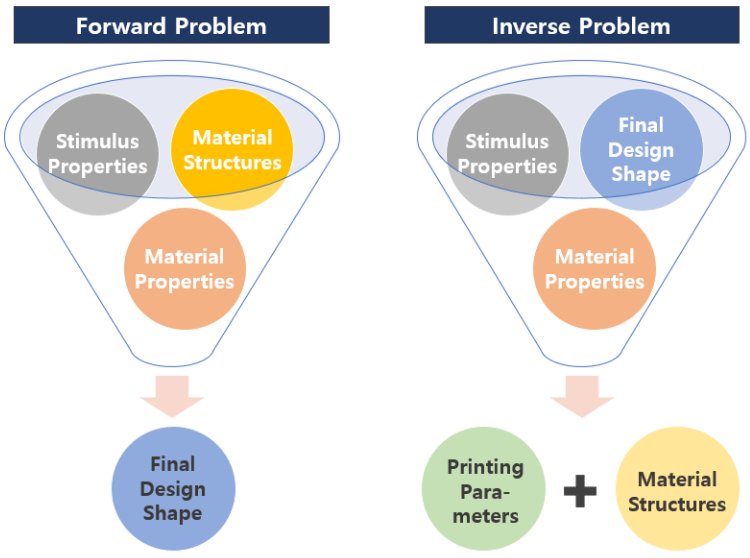

Figure 2.9 Illustration of mathematical modeling processes [3].

2.1.4 FE simulation of 4D printed part

Finite element analysis (FEA), also called finite element (FE) simulation, is a computer simulation method using the finite element method (FEM), which enables the analysis of a physical phenomenon using meshed modeling data in a short timeframe. The mechanism of a 4D printed part is a complex system that generally involves multiple materials and environmental variations. For the prediction of the behavior of a part, computer modeling and simulation can be used instead of printing all the parts to use a trial-and-error method or doing complicated mathematical calculations.

Mao et al. [22] conducted an FE simulation to predicted self-collisions of folding parts and to simulate the folding process of their 4D printed model. They developed a reduced-order model (ROM) to simulate rigid body motions (driven by the angular shape recovery of hinges) to investigate the folding pathways. They used the scaling rule to predict the shape recovery ratio of the hinge by the recovery behavior of a sample under linear stretch. In the ROM, they assumed that the angular rotation of the hinge is equal to the linear recovery ratio of an SMP. The FEA predictions were in good agreement with the measurements, although they predict slightly faster folding than the experiment, probably due to the resistance from the water in the experiment. However, there is a limit to applying their method directly to models without hinges or joint, as their simulation used the calculated rotational angle of the hinge according to the environmental change, rather than inputting the mechanical properties of the material directly.

Ge et al. [28] and Ding et al. [31] conducted an FE simulation using a multi-branch model to capture the viscoelastic shape memory behavior of SMP. In a multi-branch model, the total deformation gradient was decomposed into the mechanical deformation gradient and the thermal deformation gradient, and the mechanical deformation gradient could be decomposed again into an elastic part and a viscous part which was time and temperature dependent. The mechanical properties calculated from the multi-branch model were implemented into a user material subroutine (UMAT) in the FE simulation software to enable to prediction of the motion of the 4D printed part.

2.2 Applications of 4D Printing

4D printing is a relatively new area of research, and many researchers are working to develop new possibilities and applications for 4D printing. In this section, some areas of application for 4D printing that have already been demonstrated are introduced, along with some possible areas that 4D printing could ultimately contribute to in the future.

2.2.1 Demonstrated application of 4D printing

Biomedical field

Ge et al. [28] fabricated a 4D printed, thermo-responsive cardiovascular stent with SMP (Figure 2.10 (a)). The traditional manufacturing methods of stents have usually consisted of multiple time-consuming steps to provide the geometric complexity and resolution necessary for stents. Based on the high-resolution additive manufacturing of SMP, they [28] achieved the manufacturing of stents with various diameters, heights, numbers of joints, ligament diameters, and inter-ligament angles. Their stent was programmed into the temporary shape with a smaller diameter for minimally invasive surgery. After heating, the stent recovered into the original shape with a larger diameter.

Zarek et al. [5] 4D printed a thermo-responsive tracheal stent, which solved two of the key drawbacks in current tracheal stents (Figure 2.10 (b)). First, it gave the personalized stent structure that fitted the arcade pattern and the positioning of the cartilaginous rings, minimizing migrations of the stents. Second, the temporary form of SMP provided the low profile that prevented injurious deployment. After the insertion, the stents deployed back into its permanent shape with a local increment in temperature.

Smart Valve

Bakarich et al. [26] fabricated a smart valve that controlled the flow of water by printing robust, thermally-actuating hydrogels alongside with static materials (Figure 2.10 (c)). The flow rate of water was automatically reduced to 99% upon exposure to high temperature. When exposed to cold water, the shape of valve reversibly shifted toward closed form.

Nadgorny et al. [32] introduced pH-responsive, flow-regulating hydrogel valve that reversibly swells in an acidic solution and shrinks in an alkaline solution (Figure 2.10 (d)). They demonstrated that the degree of swelling can be precisely tuned by a choice of quaternizing reagents and their

stoichiometry.

Adaptive Meta-material

Adaptive metamaterials with tunable bandgaps enabled by 4D printing were reported by Zhang et al. [7] and later by Bodaghi et al. [14]. In both research, assemblies of tunable lattice enabled printed parts to have mechanical properties that can be adjusted based on ambient temperature. Adaptive meta-material can change their stiffness based on geometry change while the mass is constant. Therefore, they could be used as a wave switch in a particular frequency range. The structure of metamaterial developed by Zhang et al. [7] used self-folding beams in two-dimensional square lattice materials, which could reversibly transform into new configuration under processes of heating and cooling (Figure 2.10 (e)). The one reported by Bodaghi et al. [14] used a periodic arrangement of SMP actuator units, which showed a two-way planar movement of self-expanding and shrinking (Figure 2.10 (f)).

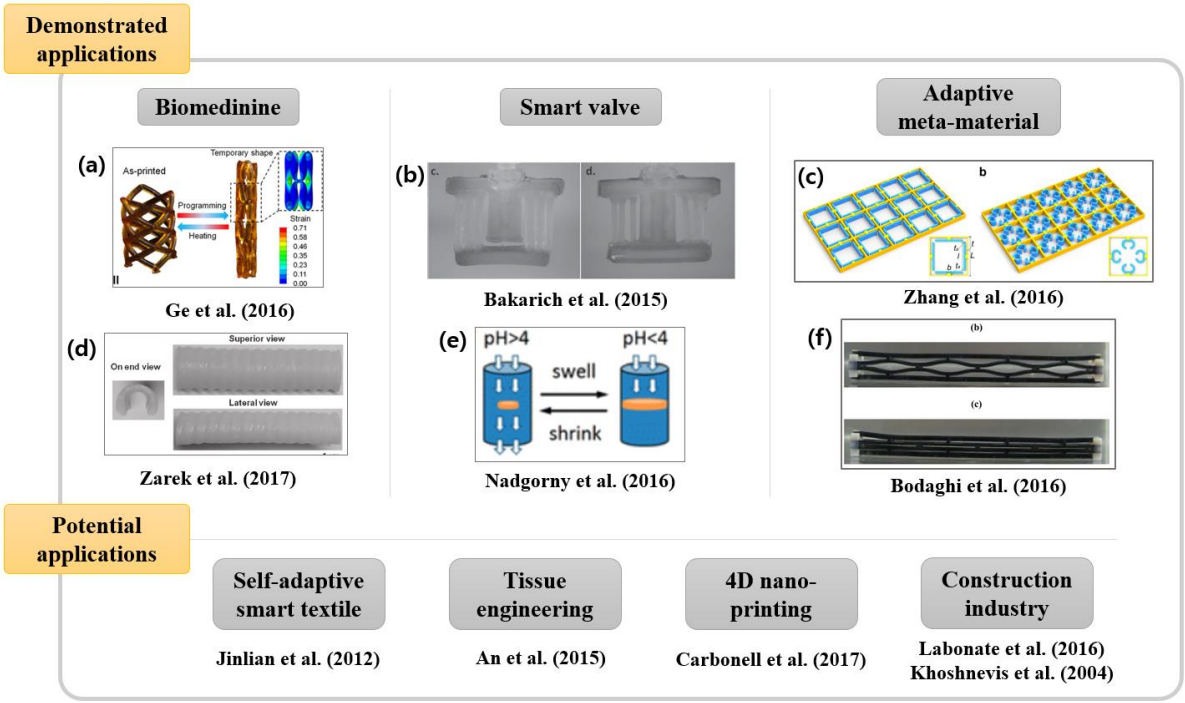

Figure 2.10 Applications of 4D Printing process.

2.2.2 Potential applications of 4D printing

4D printing of SMP material can potentially benefit the applications of self-adaptive and multi-functional textiles. In contrast to the textiles made of elastic fibers, the self-adaptive smart textile structure does not need tensile loading in order to be adapted to a new size. This feature can achieve many functions of a dress such as moisture / temperature management, wound monitoring, skin care, protection against harsh climates, or adaptive change of colors [33].

4D printing of highly porous scaffold structure can be branched out into the field of 4D bioprinting of organs and tissues [34]. The shape-shifting behavior in a 4D printed scaffold can be provided by the stimulation of stem cell differentiation.

Carbonell and Braunschweig [35] suggested the potential of a 4D nano-printing process. The control of organic materials at the nanoscale-level of spatial resolution could revolutionize the assembly of next-generation optical and electronic devices or substrates for tissue engineering or enable fundamental biological or material science investigations. Future developments in this area depend on further research on surface chemistry and instrumentation.

The additive construction of buildings has the potential to revolutionize the construction industry [36]. One of the primary technologies in this field is contour crafting (CC) [37], which is a layered fabrication technology that has a great potential in automated construction of whole structures as well as subcomponents. Khoshnevis [37] addressed that the application of CC is one of the few feasible methods for building habitats in outer space, such as Moon or Mars. Labonnote et al. [36] indicated that the smart construction using self-assembly of building blocks could be used to build infrastructure in a harsh environment where human access is difficult. Therefore, 4D printing and CC can effectively complement each other to pave the way for the human colonization of the other planets.

2.3 Multi-stable and bi-stable mechanism

Multi-stability refers to the property of having more than one equilibrium states, and bi-stability is a subset of multi-stability with only two equilibrium states [38]. Under an equilibrium state, every part of the system is at rest under zero total force. An easy example of a bi-stable system is the lever of a light switch, which is designed to hold either at the on or off position, but not between them.

The stable states of a multi-stable system are the local minima of the potential energy diagram [39], as shown in Figure 2.11. A transition from one stable state to another stable state require enough activation energy to cross the energy barrier. If a system is released before the barrier, it returns to the original stable state. If the required activation energy is reached, the system will relax into another minimum state without additional energy. The higher the barrier level, the harder it is to make a transition between different stable states.

Bi-stability has been studied in compliant mechanism for decades [38]. Compliant mechanisms refer to flexible, joint-less mechanism that transfer force or motion from input ports to output ports [40]. In general, the bi-stability of the compliant mechanism is induced by the buckling phenomena. For example, when a thin beam undergoes compression, it buckles in one of two directions normal to the beam. If a load is applied at the middle of the buckled curvature, a snap-through motion occurs, making transition from one stable state to another, as shown in Figure 2.12. The strain energy of beam buckling is calculated by the Euler-Bernoulli beam theory when the length to thickness ratio of a beam is 20 or more [41].

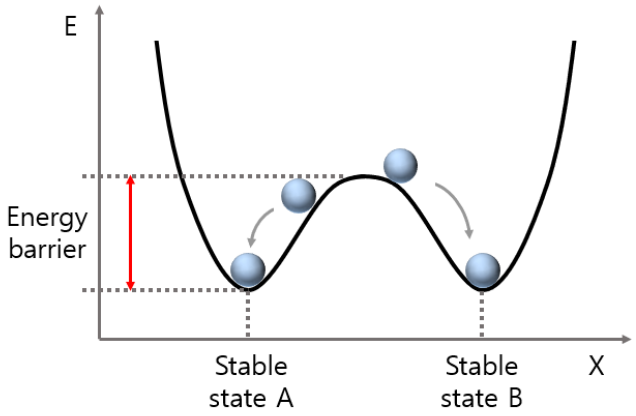

Figure 2.11 Potential energy diagram of bi-stable mechanism.

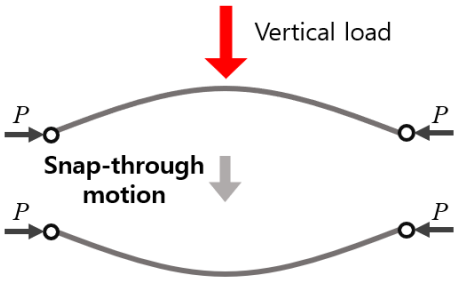

Figure 2.12 Snap-through motion of a buckled beam

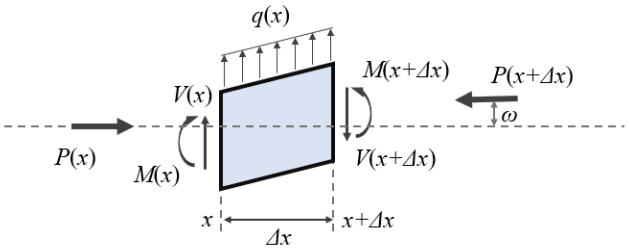

Figure 2.13 Forces and moments acting on a beam element [42].

According to the Euler-Bernoulli beam theory, the differential equation of a beam element shown in Figure 2.13 can be represented by the equation:

$$\frac{d^4\omega}{dx^4} + \frac{P}{EI}\frac{d^2\omega}{dx^2} = \frac{q}{EI}$$

where ω is the lateral deflection at position x, P is the point load, E is the elastic modulus, I is the second moment of area and q is the distributed load [42]. Solving this equation with substituting $\lambda^2 = P/EI$, the general solution of the lateral deflection of a buckled beam is the equation: $\omega(x) = Acos(\lambda x) + Bsin(\lambda x) + Cx + D$. The four constraints A, B, C, and D are determined by the boundary conditions on ω(x) at each end of the beam. In many cases, the solution of λ appears at the form $\lambda_n = n\pi/l$, for $n = 0,1,2$ .... Depending on the value on n, different buckling modes are produced, as shown in Figure 2.14. Since the load can be calculated by $P = EI\lambda^2$, the larger the buckling mode, the higher the stress of the beam element.

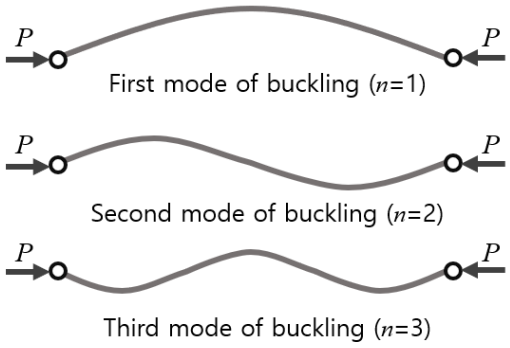

Figure 2.14 Forces and moments acting on a beam element.

In some research, FE simulation is used to predict the behavior of bi-stable or multi-stable structures [41, 43]. Jin et al. [43] used FE simulation to predict, explain and design the bi-stable behavior of two curved centrally-clamped parallel beams. They used the buckling beam theory to design a curved beam and used a mode superposition method to solve the beam deflection. Oh et al. [41] predicted the motion of a multi-stable compliant mechanism and find the load-displacement responses via nonlinear FE simulation. In their study [41], the rotatable model was used to induce buckling of connecting beams by modulating the distance of the ends of the beam.

3. FE simulation of rotatable models

To design an accurate and fast-responding 4D printed model, it is necessary to investigate the effect of the geometric parameters and mechanical properties of the materials on the performance of the model. Finite element (FE) simulation provides a reasonable investigation of the effects of variables without the extra cost or time required to 3D print all models. In this section, simulations of rotatable models with different parameters will be presented. These models are possible sub-components of the 4D printing model. Several assumptions are used to reduce computation time and improve convergence while obtaining reliable results for the simulation.

A total of 128 models are simulated to verify the effect on parameters in model geometry, material properties and temperature. The models used in this study are categorized into the pinned-pinned models, pinned-fixed models, fixed-pinned models, and fixed-fixed models, according to the method of beam connection between the rotatable inner part and the fixed outer part. The initial design of the models was done by the laboratory of Nanophotonics & Metamaterials, UNIST. Further details of FE modeling and simulation processes are discussed below.

3.1 Model description

Every model covered in this study is composed of three parts: an inner rotational part with a cross-shape, a fixed outer ring, and four beams that connect the two, as shown in Figure 3.1. The beams are the most important parts that determine the behavior of each model. Depending on how the beams are connected to the two parts, the models are classified into pinned-pinned models, fixed-fixed models, pinned-fixed models, and fixed-pinned models, as shown in Figure 3.2.

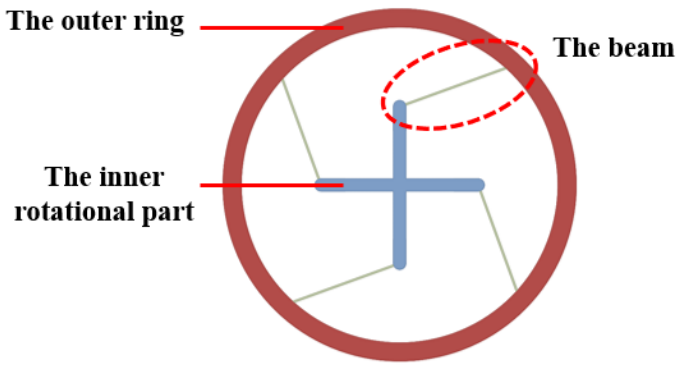

Figure 3.1 The structure of the rotatable part.

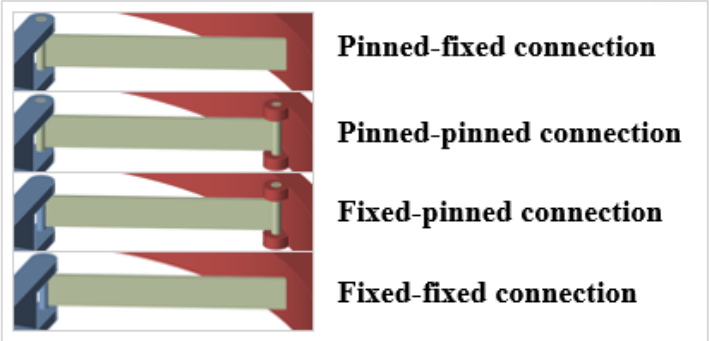

Figure 3.2 Types of beam connection in the rotatable parts.

Beams are deformed as the inner rotational part rotates while the outer ring is fixed. When a beam is pinned to the surface of the other parts while the inner rotational part rotates, the end of pinned beam rotates freely. In contrast, when the beam is fixed at the surface of the other parts while the inner part rotates, the ends of the beams maintain the angle at which they were initially connected to the rotational part. Accordingly, there are differences in the shape of the beam deflection depending on the way the beam is connected to the other parts.

Figure 3.3 shows the detailed geometry of a rotatable model. The beam is connected at an angle from the end of the inner rotational part to the inside surface of the outer ring. Thus, the length of the beams is determined by the connection angle and the radius of the inner rotational part, when the radius of the outer ring is fixed.

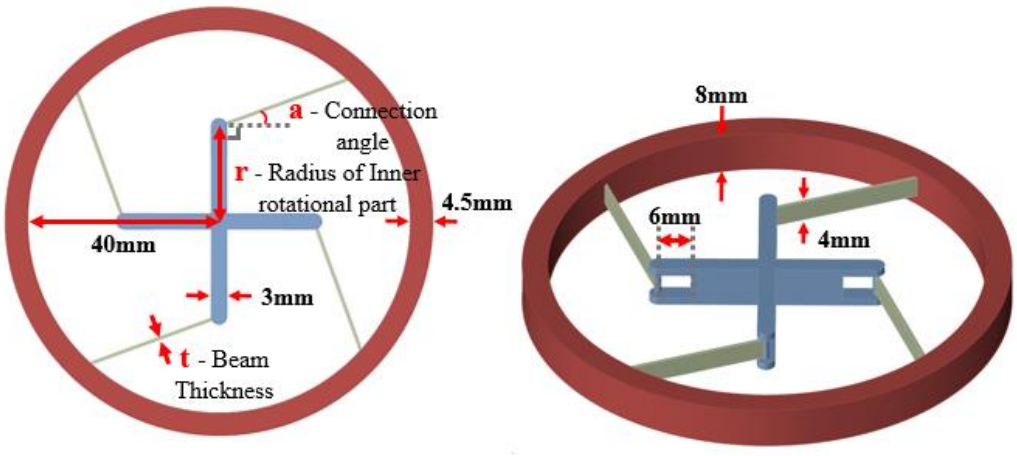

Figure 3.3 Geometry of the rotatable part.

3.2 Experimental Design

Figure 3.4 is a fishbone diagram [44] showing the factors that possibly affect the strain energy of the rotatable models used in this study. Among the presented factors, the factors related to the 3D printing process determine the quality of the output parts. However, their effect on the strain energy is relatively low, and free adjustment of parameters is limited. Among the factors included in the geometric design, both the radius of the inner rotational parts and the outer ring affect the length of the beam, but the radius of the outer ring is not considered in our list of variables because the scale of the whole part may change if the outer radius changes. The experimental factors considering these factors are shown in Table 3.1. The simulation is designed to be fully crossed using these factors.

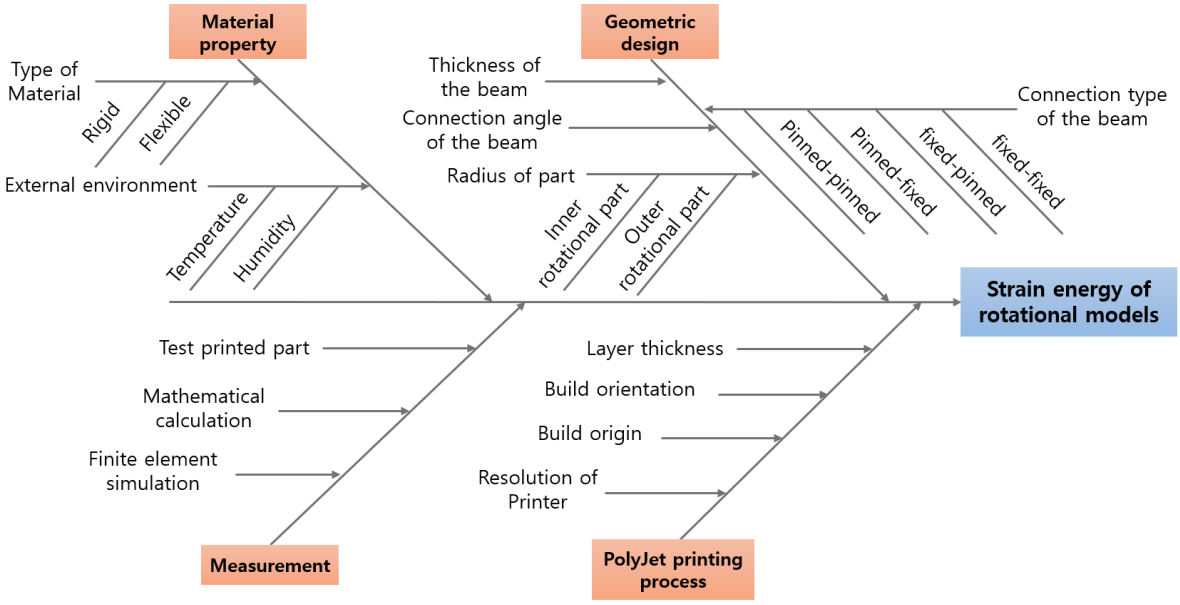

Figure 3.4 The fishbone diagram of factors affecting the strain energy.

Table 3.1 Design of Experiment

Variable	1	2	3	4
Modeling type	Pinned-pinned	Pinned-fixed	Fixed-pinned	Fixed-fixed
Radius of inner rotational part	15mm	20mm		
Connection angle	0°	20°		
Beam Thickness	0.5mm	0.9mm		
Material	Rubbery (FLEX9895-DM)	Rigid (RGD8530-DM)		
Temperature	20℃	70℃		

The strain energy *SE* at the rotation angle of the inner rotational part a_{rotate} is expressed the equation:

$$SE_{model} = SE_{model}(a_{rotate})$$

A *model* is composed of a set of factors ($C, M, T, r_{in}, a_{connect}, t_{beam}$), where *C* is the connection type of the beam, *M* is the material, *T* is the ambient temperature, r_{in} is the radius of the inner rotational part, $a_{connect}$ is the connection angle, and t_{beam} is the beam thickness. The sets of each factors are as followings:

$C = (pp, pf, fp, ff)$, $M = (rigid, rubber)$, $T = (T20, T70)$, $rin = (r15, r20)$, $a_{connect} = (a0, a20)$, $tbeam = (t0.5, t0.9)$

where *pp* means the pinned-pinned connection, *pf* is the pinned-fixed connection, *fp* is the fixed-pinned connection, and *ff* is the fixed-fixed connection. In the same way, *rigid* means the rigid material (RGD8530-DM) and *rubber* means the rubbery material (FLEX9895-DM). *T20* and *T70* are the temperature of 20℃ and 70℃, respectively. *r15* and *r20* are 15mm and 20 mm of the radius of the inner rotational part. *a0* and *a20* are 0° and 20° of the connection angles between the inner rotational part and the outer ring. Finally, *t0.5* and *t0.9* mean the beam thicknesses of 0.5mm and 0.9mm, respectively.

The names of models are composed of the elements in the sets in order of $C\text{-}M\text{-}T\text{-}r_{in}\text{-}a_{connect}\text{-}t_{beam}$. For example, a model with the following conditions: the pinned-pinned connection type, the rigid material, the temperature of 20℃, the 15mm radius of inner rotational part, the connection angle of 20°, and the beam thickness of 0.5mm, is named *pp-rigid-T20-r15-a20-t0.5*.

3.3 Finite Element Simulation Process

The following are the general processes of the FE simulation [45].

1. Input geometric information (import CAD model)
2. Generate mesh of the model.
3. Input material properties.
4. Set geometric constraints.
5. Set boundary conditions and loads.
6. Run analysis and check result.

In this section, the conditions and settings used in the FE simulation are described in detail.

3.3.1 FE simulation environment

The software used for the analysis is ABAQUS (Simulia, Providence, RI, USA). The system environment of the computer used is Intel Xeon CPU E5-2687W v3 @ 3.10GHz, RAM 128GB. Eight cores are used in the calculation. To simplify the interpretation and to assure convergence, several assumptions and model simplifications are used. Detailed descriptions are given in the following sections.

3.3.2 Mesh generation

The models described in Section 3.1 were first created as CAD files and then imported into the FE program. While the detailed geometry of the CAD model differs according to the variables mentioned in Section 3.2.5 below, the mesh generation is done in the same way for all models.

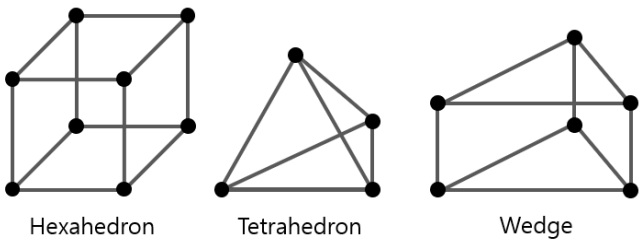

Figure 3.5 Mesh types of solid model.

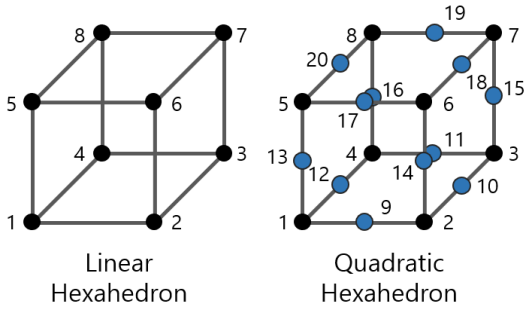

Figure 3.6 Linear and quadratic mesh types.

The mesh types used for the stress analysis of 3-dimensional solid models include hexahedron, tetrahedron, and wedge, as shown in Figure 3.5. The most commonly used mesh types of these are the hexahedral and the tetrahedral element. The tetrahedral element has the advantage of easy mesh generation for any shape of models. On the other hand, the hexahedral element has the highest solution accuracy for the same cell amount [46].

The geometric order of mesh element has two types, the linear and the quadratic, depending on the presence of a mid-side node, as shown in Figure 3.6. Although each type has its own advantages and disadvantages, the linear element with relatively fine mesh has more accuracy than the quadratic element with a relatively coarse mesh, in the nonlinear structural analysis used in this study [47].

The mesh properties of the inner rotational part and the outer ring are not considered significant because the actual results of the simulation are from the beam parts. Therefore, the element used in the mesh of the inner rotational parts and the outer ring are C3D4, which is a 4-node linear tetrahedron, as shown in Figure 3.7 (a) and (b). The grid sizes of mesh are 1.5mm in the inner rotational part and 4.5mm in the outer ring.

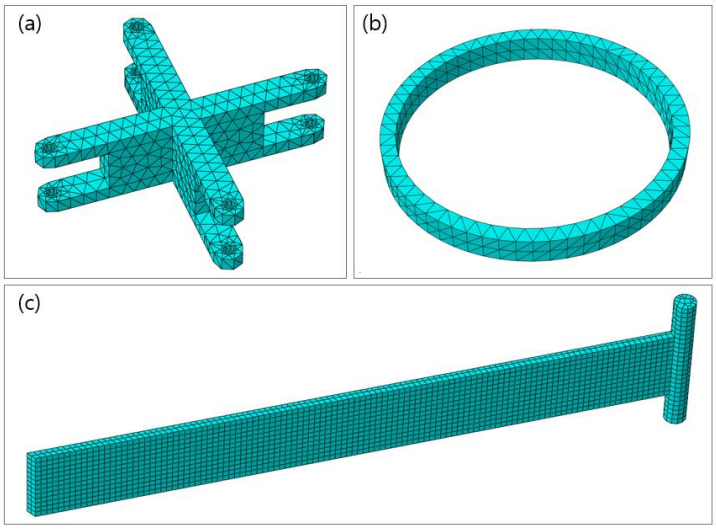

Figure 3.7 Mesh of (a) the inner rotational part. (b) the outer ring. (c) the beam part.

The element type used for the beams in all models is C3D8, which is an 8-node linear brick, as shown in Figure 3.7 (c). The reduced integration option is not used, in order to avoid the hourglass effect. The mesh size of the beam part is set to 0.3mm. The number of nodes and elements for a beam of each model with different geometry are listed in Table 3.2.

Table 3.2 The number of nodes and elements for a beam part

Number of nodes in a beam				
Models	**Pinned-pinned**	**Pinned-fixed**	**Fixed-pinned**	**Fixed-fixed**
r15-a0-t0.5	6594	6230	6566	5292
r15-a0-t0.9	8204	7840	8148	7112
r15-a20-t0.5	5894	5277	7784	5277
r15-a20-t0.9	7448	8424	7392	8397
r20-a0-t0.5	8176	5490	8120	5571
r20-a0-t0.9	7756	8860	7812	8914
r20-a20-t0.5	7028	4731	6832	3990
r20-a20-t0.9	6664	7514	6496	7417
Number of Elements in a beam				
r15-a0-t0.5	4227	3979	4200	3250
r15-a0-t0.9	5772	5481	5718	4914
r15-a20-t0.5	3784	3328	5568	3328
r15-a20-t0.9	5283	6240	5229	6214
r20-a0-t0.5	5826	3432	5772	3510
r20-a0-t0.9	5460	6552	5514	6604
r20-a20-t0.5	5034	2990	4845	2444
r20-a20-t0.9	4772	5564	4560	5486

3.3.3 Material property and assumption

For the simplification of the analysis, the material properties of all the materials used in the simulation are assumed to be isotropic and elastic. Plus, the arrangement of the material is assumed to be homogeneous. As materials are added in a layer-by-layer manner in actual 3D printing, there is a difference in mechanical properties between the x and y-direction and the z-direction [48]. However, since there is no load or displacement in the z-direction in this simulation, the assumption that the material is isotropic and homogeneously arranged does not affect the results.

The mechanical properties of the materials are measured using dynamic mechanical analysis (DMA) from the laboratory of Nanophotonics & Metamaterials, UNIST, then imported into the FE simulation program. As listed in Table 3.3, the elastic modulus of material E_{mat} of the rigid material (RGD8630-DM) is 1474MPa at T=20°C and 15.8MPa at T=70°C. E_{mat} of the rubbery material (FLEX9895-DM) is 253MPa and 3.7MPa at T=20°C and at T=70°C, respectively. The density of both materials is 1.15×10^{-9}mm^3/ton. The rigid material is applied to the inner rotational part and the outer ring of all models. The beam parts of models were applied with either rigid material or rubbery material, depending on the simulation models.

Table 3.3 Material properties used in the simulation

Material	Elastic Modulus		Density	Poisson ratio
	T=20°C	T=70°C		
Rigid (RGD8530-DM)	1474MPa	15.8MPa	1.15x10^{-9} ton/mm^3	0.3
Rubbery (FLEX9895-DM)	253.3MPa	3.7MPa	1.15x10^{-9} ton/mm^3	0.3

3.3.4 Constraint and analysis setting

This section describes the geometric constraints and boundary conditions for each model, as well as additional options for improving convergence.

Since the deformation in the inner rotational parts and the outer ring are small enough to be neglected, they are both set as rigid bodies. A rigid body is constrained to displacement or rotation about a corresponding reference point. As shown in Figure 3.8, two reference points, RP1 and RP2, are created at the middle point of the inner rotational part. The inner rotational part is constrained to RP1, and the outer ring is constrained to RP2.

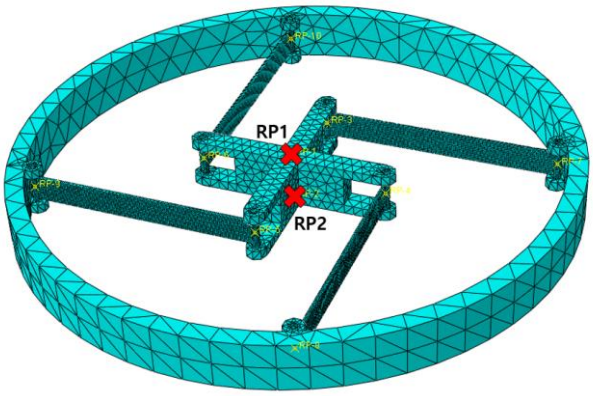

Figure 3.8 Reference points for the inner rotational part and the outer ring.

Instead of the contact condition, the pinned connection between a rotational part and beam part is constrained using a beam type MPC constraint, for simplification of the simulation. Also, the friction is ignored in the simulation model. A beam-type MPC constraint allows slave surfaces tied to a master point. For master points, the reference points are created at the center of each pin where the rotational part is connected to the beam. They are designated as RP3-RP6 in the pinned-fixed and the fixed-pinned model, and RP3-RP10 in the pinned-pinned model. To allow these reference points to rotate together when the inner rotational part rotates, or to be fixed together with the outer ring, they are set as pins in the setting for the rigid body constraint in the inner rotational part and the outer ring. For slave surfaces, the cylindrical surfaces of beam ends are selected, as shown in Figure 3.9 (a).

The fixed connection between a rotational part and beam part is directly established using tie constraint. The surfaces of rigid bodies are set to be master surfaces because rigid bodies cannot be penetrated. The surface of the end of the beam is set to be slave surface of the corresponding master surface, as shown in Figure 3.9 (b).

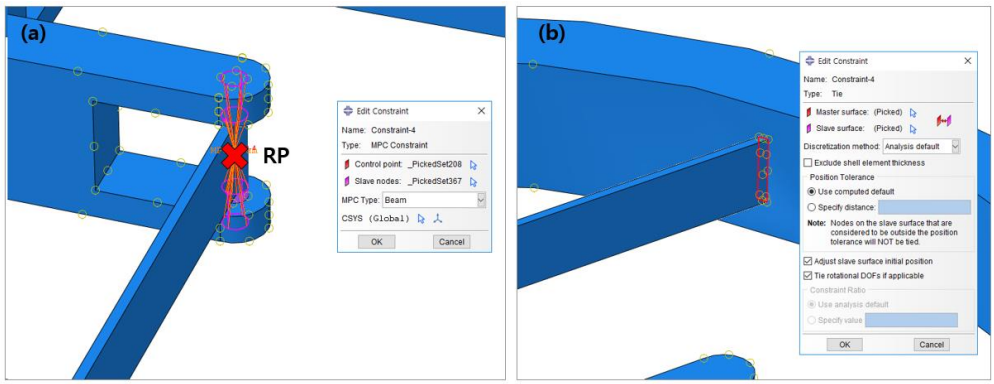

Figure 3.9 Constraints settings for (a) the pinned connection. (b) the fixed connection.

Several steps with different load and boundary conditions are created for the process of the simulation. The type of every step is set to static general. Static and implicit steps are more suitable for this simulation, despite the fact that rotating an actual part is a dynamic movement. Dynamic and explicit steps are used when there is fast movement, collision, or complex contact. Instead, in this simulation, the part is slowly rotated to observe the strain energy and deformation of the part in each angle. For the same reason, instead of using the actuation moment to rotate the part, a method of applying a constant angular velocity to the inner rotational part is adopted in the simulation. Also, the Nlgeom (non-linear geometry) option is used to include a large-deflection effect in all steps.

At the moment when the part begins to rotate from a stationary state, the elements of the beam move very unstably, as the velocity of elements suddenly accelerates from zero velocity. This causes a solution to fail to convergence and to distort geometries into an abnormal shape. To avoid these problems, the automatic stabilize option is used for each step. This option adds a damping effect to the velocity change of the part, preventing speed from changing rapidly [45].

The simulation process for the fixed-fixed model is set with three steps. The first step (initial step) predefines the boundary condition that is applied throughout the analysis. The second step (Step 1) is for rotating the inner rotational part in the direction in which the beams are deflected. In the third step (Step 2), it is rotated in the opposite direction, continuing until the beam is stretched past the original stable point. This is done in order to obtain the result of the rotational angle in the negative value.

The specific settings of each step in the fixed-fixed model are shown in Table 3.4. In the initial step, RP2 is encastre so that the outer ring is fixed throughout the simulation. In Step 1, the reference point of the inner rotational part (RP1) is rotated at 1.0 rad/sec in the -z-direction. The duration time of Step 1 is determined by considering the possible rotation angle of each model. In Step 2, RP1 rotates in the opposite direction (+z) at same angular velocity, and the duration time is set to be 0.1 seconds longer than that of Step 1, the rotational direction is shown in Figure 3.10.

The simulation processes for the pinned-pinned model, the pinned-fixed model, and the fixed-pinned model are slightly different from those of the fixed-fixed model, since the convergence of the analysis is decreased if the beam is deflected in an inappropriate direction at the beginning of the simulation. After the initial step of constraining the outer ring, a step (Step 1) is added to determine the trajectory of the beam deflection. In the next step (Step 2), the inner rotational part is rotated in the direction in which the beams are deflected. The fourth step (Step 3) is for rotating it in the opposite direction.

The detailed settings of steps are shown in Table 3.5. In the initial step, RP2 is fixed, which is

continued throughout the analysis. In Step 1, the moment of 0.01N·mm is applied to RP3-6 in the +z-direction for 0.01 second, so that the directions in which the beams are initially deflected are aligned with the rotational direction of the inner rotational part. Since this step is short and the moment is also small, it has little effect on the results of the simulation. However, this process is necessary to reduce the problem that in which energy of the beam becomes abnormally high or the solution does not converge, due to the drastic energy change that happens when the beams bend in the inappropriate trajectory at the beginning of the simulation. Thereafter, in Step 2, RP1 is rotated at a rate of 1.0 rad/sec in the -z-direction to deflect the beam. In a similar wat to the two models above, the duration of the step is maintained until the rotation angle passes beyond the second stable point. In Step 3, the direction of the angular velocity of RP1 is inversed to the +z direction and the rotation is continued for the duration time of 0.1 seconds longer than the duration of Step 2.

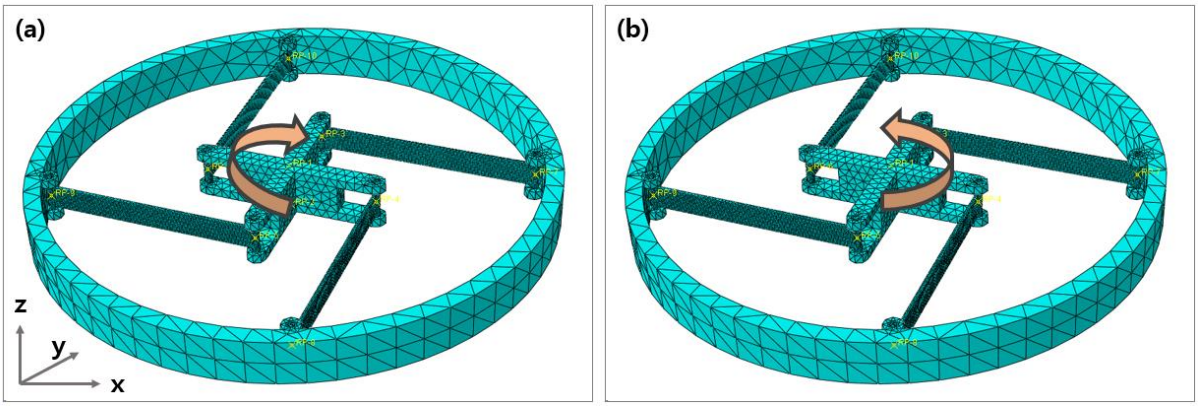

Figure 3.10 Rotational direction in (a) -z-direction. (b) +z-direction.

Table 3.4 Step settings for the fixed-fixed model

Step Setting			
	Initial step	**Step 1**	**Step 2**
BC1 : Fix RP2	Created	Continued	Continued
BC2 : Rotate RP1 in 1rad/sec	-	Created -z-direction	Modified +z-direction
Duration times for the fixed-fixed model (sec)			
r15-a0	-	1.9	2
r15-a20		1.6	1.7
r20-a0		1.9	2
r20-a20		1.4	1.5

Table 3.5 Step settings for the pinned-pinned, pinned-fixed, and fixed-pinned model

Step Setting				
	Initial step	**Step 1**	**Step 2**	**Step 3**
BC1 : Fix RP2	Created	Continued	Continued	Continued
Load case 1: Rotate pinned beam at 0.01N·mm	-	Created z-direction	Removed	Removed
BC2 : Rotate RP1 in 0.01rad/sec	-	-	Created -z-direction	Modified +z-direction
Duration times for the pinned-pinned model (sec)				
r15-a0	-	0.01	2.4	2.5
r15-a20			1.9	2
r20-a0			2.2	2.3
r20-a20			1.9	2
Duration times for the pinned-fixed model (sec)				
r15-a0	-	0.01	2.45	2.55
r15-a20			1.9	2
r20-a0			2.2	2.3
r20-a20			1.45	1.55
Duration times for the fixed-pinned model (sec)				
r15-a0	-	0.01	2.3	2.4
r15-a20			1.7	1.8
r20-a0			2.3	2.4
r20-a20			1.5	1.6

3.4 Results and analysis

This section describes result of the beam deflection and the strain energy derived from the FE simulations performed for each model. Only the characteristic features of each model and the difference according to the variables will be described in this section, and the results for all simulations are available in the Appendix.

3.4.1 Behavior

In this section, the behavior of the beams in the FE simulation result is analyzed. The beams of the model used in this study can be explained by the Euler-Bernoulli beam theory because they have the form of a thin beam whose thickness is less than 1/20 of the length. As the inner rotational part rotates, the movement of the beam is similar to a buckling phenomenon under the compressive load or moment. Therefore, the behavior of the beam will be explained in terms of the buckling mode in this section [49].

In the simulation results, the beam deflections of the models are mostly in the form of mode-1 buckling. Figure 3.11-3.14 show the shape of beam deflection in mode-1 buckling in the beam connection type of the pinned-pinned model, the pinned-fixed model, the fixed-pinned model, and the fixed-fixed model, respectively. The beams of the pinned-pinned model are bent in a shape of sine-curve, which is symmetric to the midpoint and concave with respect to the direction of rotation. In the case of the pinned-fixed model, the direction of convexity is same as the pinned-pinned model, but the most curved parts of beams are relatively shifted toward the inner rotational part as compared with the pinned-pinned model.

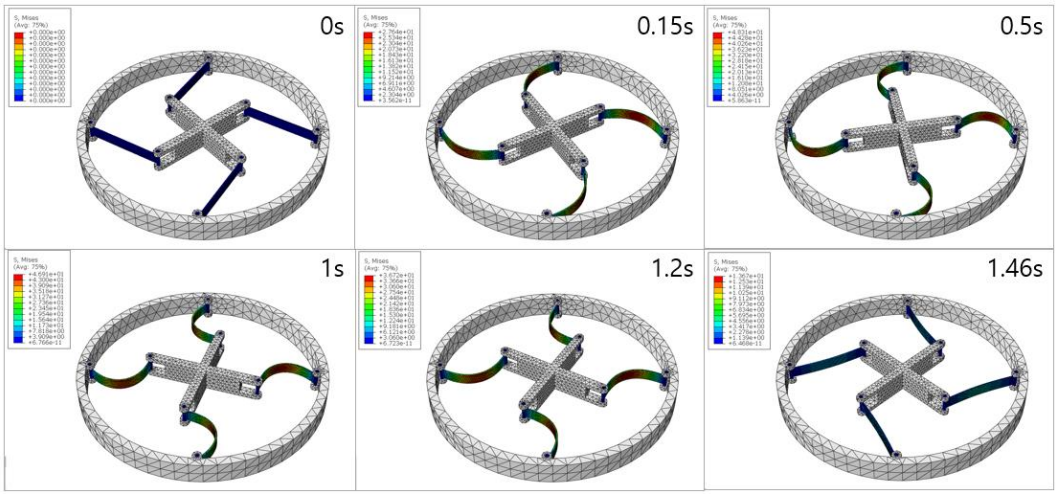

Figure 3.11 Beam deflection in the pinned-pinned model (*pp-rigid-T20-r20-a20-t0.5*).

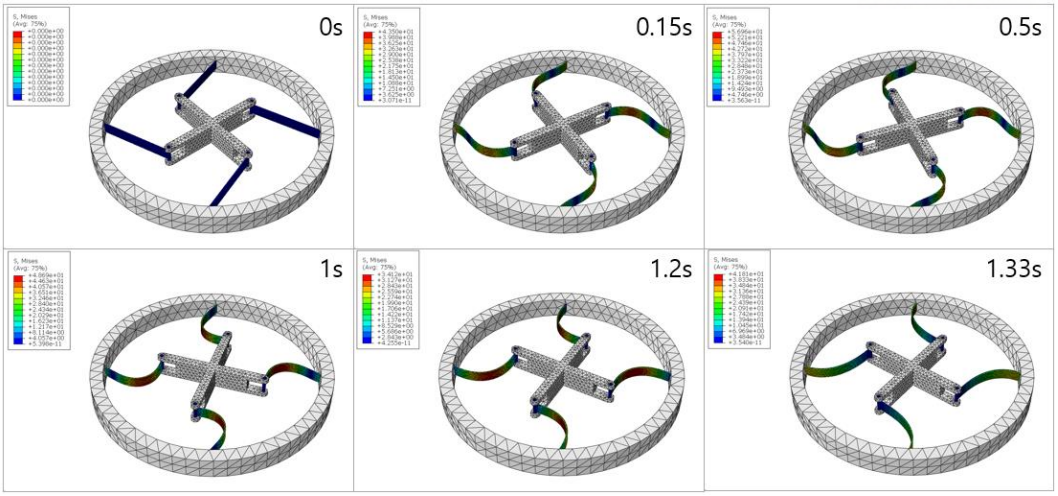

Figure 3.12 Beam deflection in the pinned-fixed model (*pf-rigid-T20-r20-a20-t0.5*).

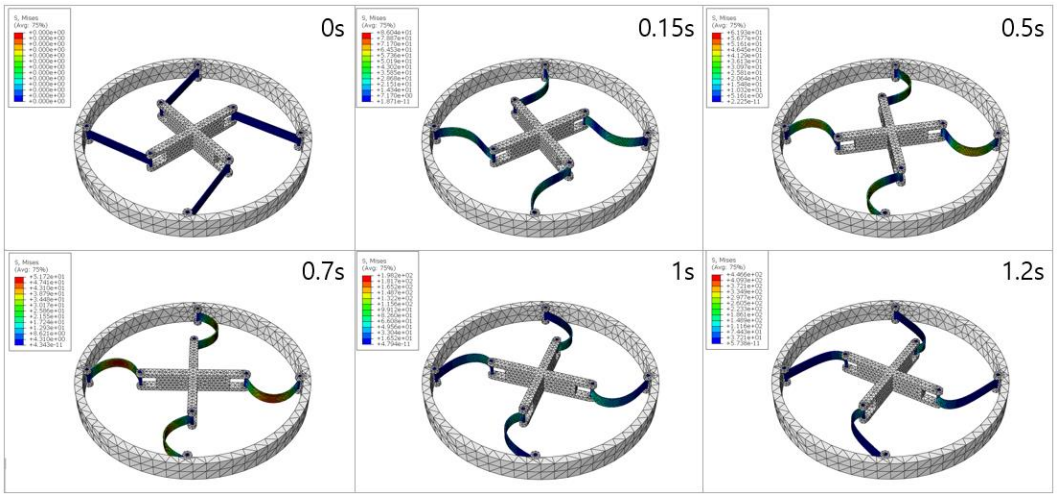

Figure 3.13 Beam deflection in the fixed-pinned model (*fp-rigid-T20-r20-a20-t0.5*).

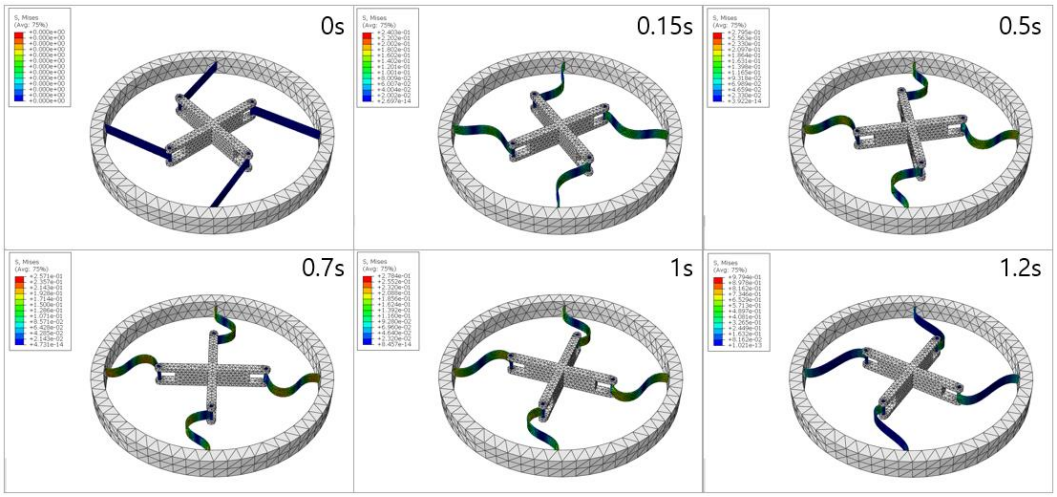

Figure 3.14 Beam deflection in the fixed-fixed model (*ff-rigid-T70-r20-a20-t0.5*).

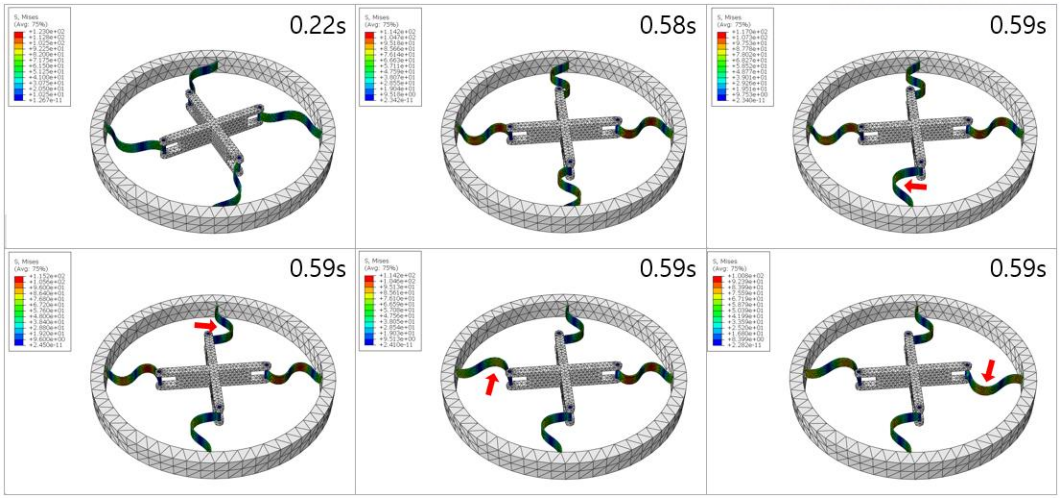

Figure 3.15 Snap-through motion in the fixed-fixed model (*ff-rigid-T20-r20-a20-t0.5*).

On the other hand, in the fixed-pinned model, the direction of convexity is opposite to the two models above, and the most curved part shifts toward the outer ring when the rotation started. As the rotation angle is increased, the curve becomes symmetrical, and then it shifts toward the inner rotational part. In the fixed-fixed model, deflected beams have a shape similar to the cosine curve, which is almost symmetric to the midpoint while the rotation angle is small. As the rotation angle is increased, the curve moves toward the inner rotational part.

Although the models mostly show mode-1 buckling behavior, some of the models have different behaviors as the rotation angle is increased. The characteristic feature of these models is that the beams are deflected in the form of mode-1 buckling, but in the opposite direction to most other models. In this case, as the rotation angle increases, the beam deflection gradually changes to the shape of the mode-2 buckling. Then, a snap-through motion occurs at a specific rotational angle, which is for changing the beam deflection in the opposite direction, as shown in Figure 3.15. This snap-through motion is difficult to predict due to the high nonlinearity, which makes the simulation hard to converge. The step increment time should be reduced to converge this model, which results in an increase in the computation time. However, when models showing the snap-through motion are rotated back to +z-direction after they have been rotated to the endpoint, they have the same beam deflection as most models.

3.4.2 Strain energy

As mentioned in Section 2.3, the bi-stability of the models can be predicted by examining the strain energy of the deflected beams. A slope in the strain energy graph is proportional to the reaction moment of a part. The point at which the slope of the strain energy curve becomes zero is the point at which the part is at rest when an external force is not applied. Mathematically, that can be either the local maxima or local minima of the strain energy graph. However, the beam at local maxima can move to other stable states, which are the local minima, with a minimal external load. Therefore, the local minima of the strain energy curve mean the stable states or equilibrium states, and the local maxima mean the energy barriers between two local minima. In this section, the strain energy to the rotation angle of each model will be analyzed by comparing them to the behavior shown in Section 3.4.1. Also, the energy level and bi-stability according to the variable in the models will be discussed.

The strain energy and the rotation angle are expressed by the following equation:

$$SE_{stable1} = SE(a_{rotate,stable1}) = SE_{min,1} = SE(a_{rotate} = 0)$$

$$SE_{stable2} = SE(a_{rotate,stable2}) = SE_{min,2} = min(SE(a_{rotate})), \quad for\ a_{rotate} > 0$$

$$SE_{barrier} = SE_{max} - SE_{stable2} = max(SE(a_{rotate})) - SE_{stable2}, \quad for\ 0 < a_{rotate} < a_{rotate,stable2}$$

$$SE_{inflect} = SE(a_{rotate,inflect})$$

Where SE is the strain energy at the rotation angle of the inner rotational part a_{rotate}, and $SE_{stable1}$ and $SE_{stable2}$ are the strain energy at $a_{rotate,stable1}$ and $a_{rotate,stable2}$, the rotation angles at two stable states. $SE_{barrier}$ refers to the energy needed to make transition from the second stable state to the original stable state. $SE_{inflect}$ is the strain energy at the inflection point of strain energy curve, and $a_{rotate,inflect}$ is the corresponding rotation angle of the inner rotational part.

First, the strain energy graph in most of the models that do not show the snap-through motion will be explained. The strain energy graphs of the pinned-pinned model and the pinned-fixed model have two local minima, as shown in Figure 3.16 (a). In contrary, the fixed-fixed model and the fixed-pinned model have a single local minimum, as shown in Figure 3.16 (b). This means that the first two models have bi-stability and the latter two models do not have bi-stability.

In the pinned-pinned model, $SE_{stable2}$ has a value of zero, the same as $SE_{stable1}$. Also, the strain energy curve between two stable states shows a symmetric shape to the midpoint. This is because the beam is in the same flat shape in both stable states, and it is not under stress in the second stable state. On the other hand, in the pinned-fixed model, the beam is deflected in the second stable state. Thus, in the pinned-fixed model, $SE_{stable2}$ is higher than 0, and the shape of the curve is asymmetric. This means that the transition from the original stable state to the second stable

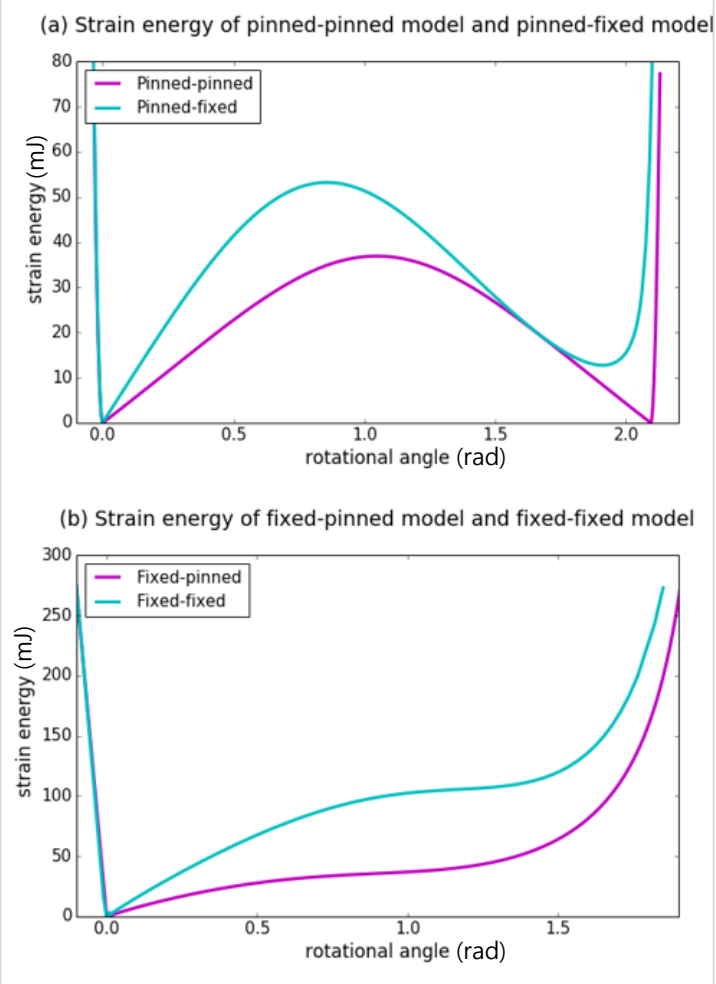

Figure 3.16 Strain energy graphs of (a) the pinned-pinned model and the pinned-fixed model. (b) the fixed-fixed model and the fixed-pinned model (*rigid-T20-r20-a0-t0.5*).

state requires a higher amount of energy than the transition of in opposite direction.

As shown in Figure 3.16 (b), a comparison of the strain energy graphs of two models with no bi-stability shows that the strain energy level is higher in the fixed-fixed model than in the fixed-pinned model under the same a_{rotate}. The strain energy graphs of both models have inflection points, where the curve changes from convex to concave. This means that if the a_{rotate} exceeds the point, *SE* increases rapidly.

Next, the strain energy graph in the cases which showed snap-through motion presented in Section 3.4.1 will be discussed. In the example of the *ff-rigid-T20-r20-a20-t0.5* model, the snap-through motions of the four beams occurred in an instant at the time t=0.59s, as shown in Figure 3.15. The strain energy graph of this model is shown in the Figure 3.17. As can be seen in the graph, *SE* shows a sharp drop at the point of the snap-through motion. If I compare the strain energy curve symmetrically from the center, it can be seen that the *SE* in the left side increases at a higher slope at the beginning of rotation, then decreases sharply to recover the same phase as the right side. This means that *SE* is higher while the beams deflect in the opposite direction and

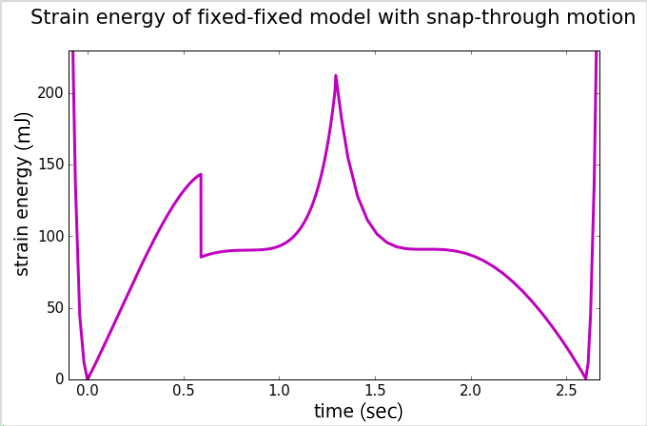

Figure 3.17 Strain energy graph of the fixed-fixed model (*rigid-T20-r20-a20-t0. 5*).

undergo the mode-2 buckling, and the snap-through motion stabilizes the abnormally high *SE*.

The strain energy curve, in this case, has two local minima, but it does not mean bi-stability in the model. This is because, even if the beam is moving to a more stable state, it is only a process of restoring stability from the inappropriate or excessive buckling. If the external load is removed from the model at this local minimum position, the model will rotate to $a_{rotate,stable1}$ instead of staying at the position. This can be expected from the right side of the strain energy curve in Figure 3.17, which has only one local minimum.

Statistical analysis was used to determine the relationship between the variables in the models and the strain energy levels, using commercial tool Minitab® (Minitab Inc., State College, PA, USA). It was conducted separately for models with and without bi-stability because the models have different utilities. For two models with bi-stability, $a_{rotate,stable2}$ and $SE_{barrier}$ were analyzed. In the case of the two models without bi-stability, $a_{rotate,inflect}$ and $SE_{inflect}$ were analyzed.

Table 3.6 ANOVA result for $a_{rotate,stable2}$ of the pinned-pinned model and the pinned-fixed model

Source	DF	Adj SS	Adj MS	F-Value	P-Value
material	1	0.01283	0.01283	3.84	0.056
temperature	1	0.02015	0.02015	6.03	0.018
radius	1	1.19870	1.19870	358.69	0.000
angle	1	6.14827	6.14827	1839.78	0.000
thickness	1	0.00203	0.00203	0.61	0.439
connection type	1	0.35308	0.35308	105.65	0.000
Error	50	0.16709	0.00334		
Total	62	7.93930			

S	R-sq	R-sq(adj)	R-sq(pred)
0.0578087	97.90%	97.39%	96.67%

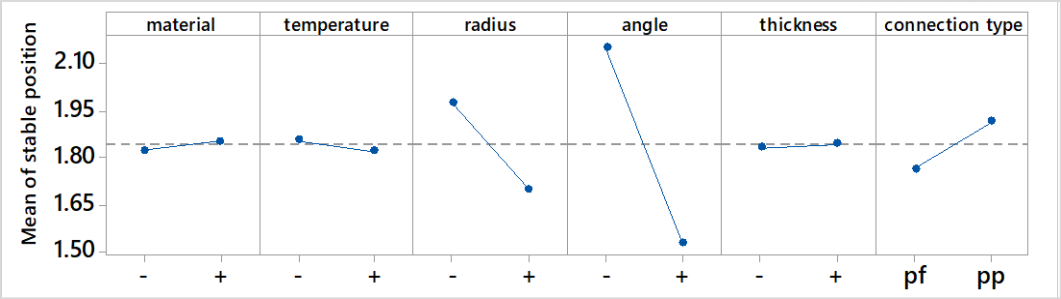

Figure 3.18 Main effects plot for $a_{rotate,stable2}$ of the pinned-pinned model and the pinned-fixed model.

Table 3.6 shows the ANOVA result of $a_{rotate,stable2}$ for the two models with bi-stability, i.e., the pinned-pinned and the pinned-fixed models. The p-values of the temperature (T), radius of the inner rotational part (r_{in}), beam connection angle ($a_{connect}$), and beam connection type are found to be less than 0.05, which means they affect $a_{rotate,stable2}$. Especially, r_{in}, $a_{connect}$ and the connection type have more significant influence on the stable position than the other variables, inferred from their p-values and slopes in the main effects plot in Figure 3.18. The lower T, r_{in}, and $a_{connect}$ result in the higher $a_{rotate,stable2}$. Besides, the pinned-pinned connection type has larger $a_{rotate,stable2}$ than the pinned-fixed connection type, as shown in Figure 3.18.

Table 3.7 ANOVA result for $SE_{barrier}$ of the pinned-pinned model and the pinned-fixed model

Source	DF	Adj SS	Adj MS	F-Value	P-Value
material	1	71402	71402	14.34	0.000
temperature	1	108125	108125	21.72	0.000
radius	1	4328	4328	0.87	0.355
angle	1	6573	6573	1.32	0.256
thickness	1	69830	69830	14.03	0.000
connection type	1	6477	6477	1.30	0.259
Error	53	263833	4978		
Total	62	723222			

S	R-sq	R-sq(adj)	R-sq(pred)
70.5548	63.52%	57.33%	48.57%

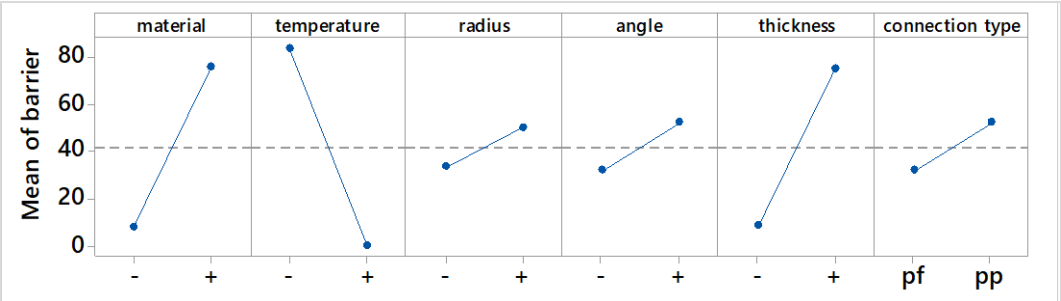

Figure 3.19 Main effects plot for $SE_{barrier}$ of the pinned-pinned model and the pinned-fixed model.

Table 3.7 shows the ANOVA result of $SE_{barrier}$ for the two models with bi-stability. The p-values of the material (E_{mat}), the temperature (T), and the beam thickness (t_{beam}) are nearly zero, which means they have considerable influence on $SE_{barrier}$. As shown in Figure 3.19, the effect of three variables shows clear relationship with the strain energy level. The lower T and the higher E_{mat} and t result in the higher $SE_{barrier}$. The rest three variables also show positive slope in the main effect plot, but there are definite differences in impacts between the former and the latter.

Figure 3.20 (a)-(f) are strain energy graphs showing examples of the results for the above statistical analysis. Compared to the *pp-rigid-T20-r15-a0-t0.5* model, the strain energy graphs of each model with different connection type, E_{mat}, T, r_{in}, $a_{connect}$, and t_{beam} are shown. E_{mat}, T and t_{beam} had a significant effect on the strain energy level. The models with lower T and the higher E_{mat} and t_{beam} have the higher scales of SE. The beam connection type, r_{in}, and $a_{connect}$ affected $a_{rotate,stable2}$. The models with smaller r_{in} and $a_{connect}$ shows the higher $a_{rotate,stable2}$. The pinned-pinned model shows larger $a_{rotate,stable2}$ than the pinned-fixed model.

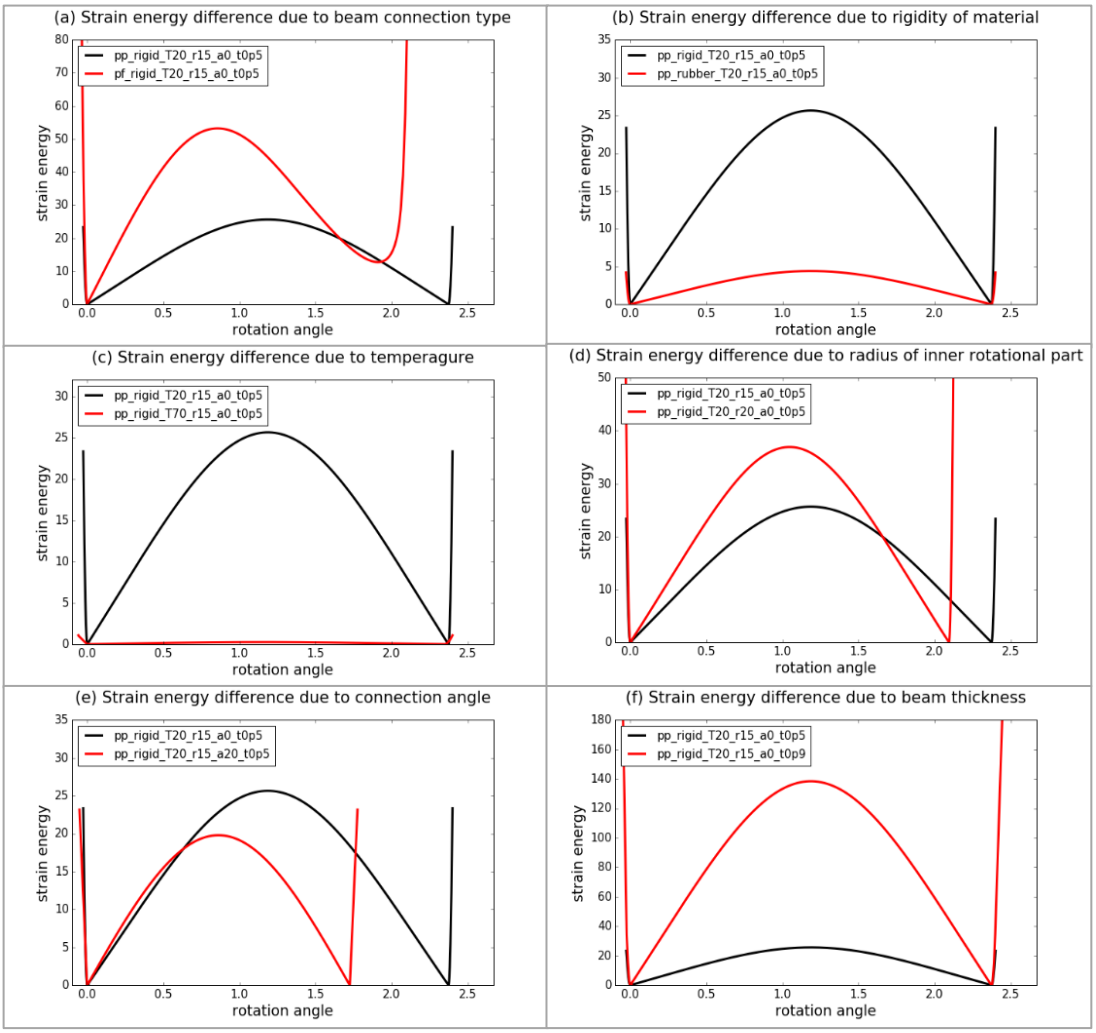

Figure 3.20 Strain energy graphs for comparing the *pp-rigid-T20-r15-a0-t0.5* with different (a) the beam connection type. (b) E_{mat}. (c) T. (d) r_{in}. (e) $a_{connect}$. (f) t_{beam}.

Table 3.8 ANOVA result of $a_{rotate,inflect}$ for the fixed-fixed model and the fixed-pinned model

Source	DF	Adj SS	Adj MS	F-Value	P-Value
material	1	0.00001	0.00001	0.00	0.983
temperature	1	0.00497	0.00497	0.24	0.625
radius	1	0.01712	0.01712	0.83	0.366
angle	1	2.25348	2.25348	109.71	0.000
thickness	1	0.77576	0.77576	37.77	0.000
connection type	1	1.36780	1.36780	66.59	0.000
Error	50	1.02706	0.02054		
Total	62	6.84190			

S	R-sq	R-sq(adj)	R-sq(pred)
0.143322	84.99%	81.39%	76.24%

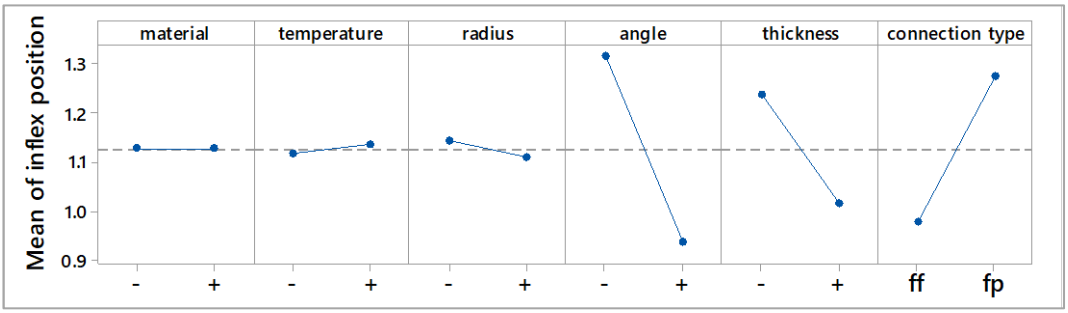

Figure 3.21 Main effects plot for $a_{rotate,inflect}$ of the fixed-fixed model and the fixed-pinned model.

Table 3.8 shows the ANOVA result of $a_{rotate,inflex}$ for the two models without bi-stability, i.e., the fixed-pinned and the fixed-fixed models. The p-values of $a_{connect}$, t_{beam}, and the beam connection type are nearly zero, which means the significant effect on $a_{rotate,inflex}$. As shown in Figure 3.21, $a_{rotate,inflex}$ is proportional to $a_{connect}$ and t_{beam}. Besides, the fixed-pinned connection type has larger $a_{rotate,stable2}$ than the fixed-fixed connection type.

Table 3.9 ANOVA result of $SE_{inflect}$ for the fixed-fixed model and the fixed-pinned model

Source	DF	Adj SS	Adj MS	F-Value	P-Value
material	1	103841	103841	35.91	0.000
temperature	1	197769	197769	68.40	0.000
radius	1	9534	9534	3.30	0.075
angle	1	1540	1540	0.53	0.469
thickness	1	52643	52643	18.21	0.000
connection type	1	22538	22538	7.79	0.007
Error	50	144570	2891		
Total	62	768933			

S	R-sq	R-sq(adj)	R-sq(pred)
53.7718	81.20%	76.69%	70.02%

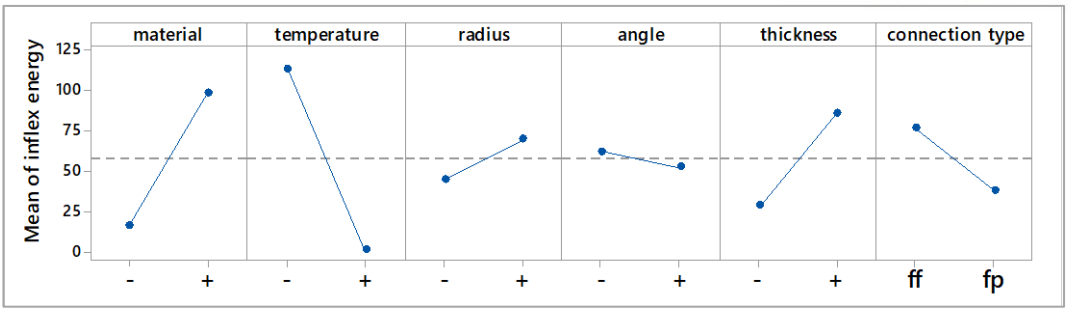

Figure 3.22 Main effects plot for $a_{rotate,inflect}$ of the fixed-fixed model and the fixed-pinned model.

Table 3.9 shows the ANOVA result of $SE_{inflect}$ for the two models without bi-stability. The p-values of the E_{mat}, T, t_{beam}, and the beam connection type are found to be less than 0.05, which means they affect $a_{rotate,stable2}$. Among them, the p-values of E_{mat}, T and t_{beam} are close to zero. Besides, the effect of r_{in} should not be completely ignored, since it has p-value close to 0.05. As shown in the main effect plot in Figure 3.22, E_{mat} and t_{beam} show proportional effect, and T and the connection type have inverse proportional effect.

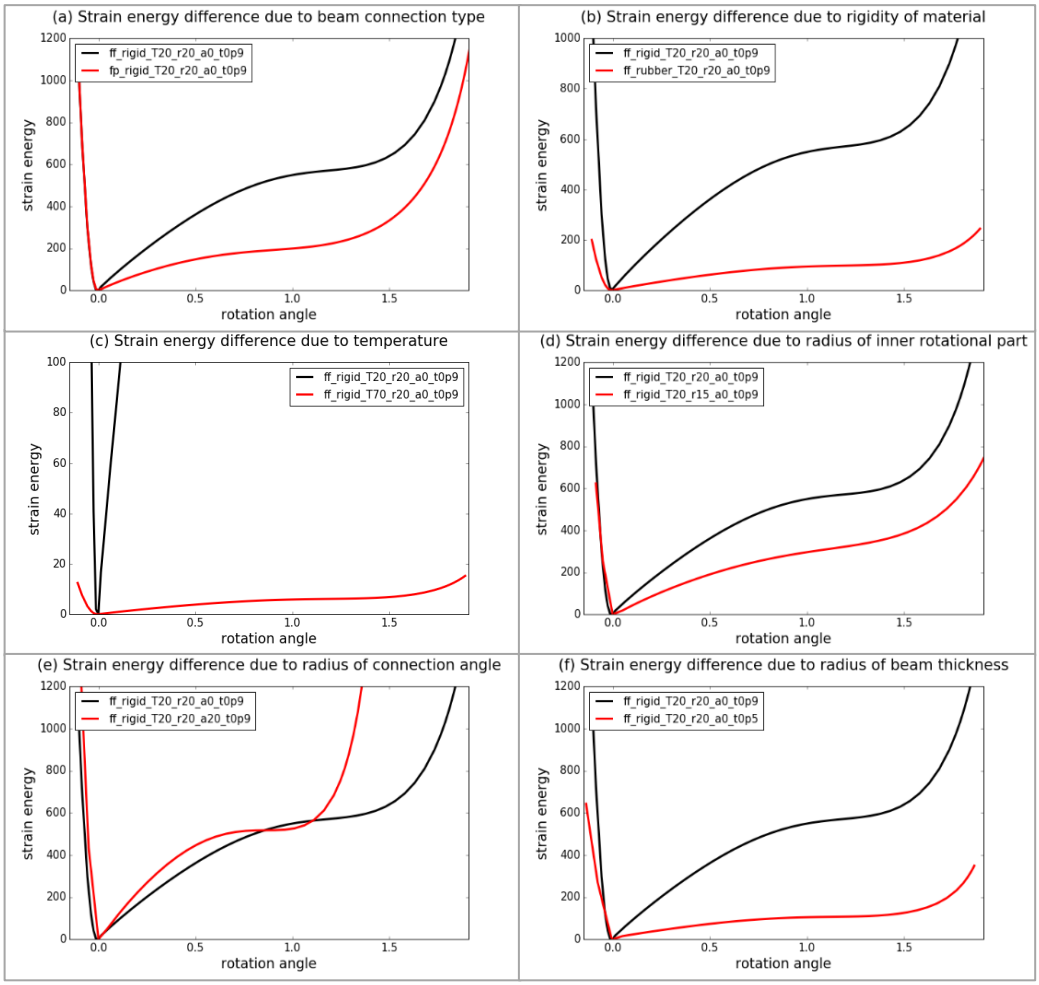

Figure 3.23 Strain energy graphs for comparing *ff-rigid-T20-r20-a0-t0.9* with different (a) the beam connection type. (b) E_{mat}. (c) T. (d) r_{in}. (e) $a_{connect}$. (f) t_{beam}.

Figure 3.23 (a)-(f) are strain energy graphs showing examples of the results for the above statistical analysis. Compared to the *ff-rigid-T20-r15-a0-t0.9* model, the strain energy graphs of each model with different connection type, E_{mat}, T, r_{in}, $a_{connect}$, and t_{beam} are shown. E_{mat}, T and t_{beam} have a significant effect on the strain energy level. The models with lower T and the higher E_{mat} and t have the higher scales of SE. Also, r_{in} and $a_{connect}$ affected the position of second stable state enough to be aware. The models with smaller $a_{connect}$ and t_{beam} shows the higher $a_{rotate,inflect}$. The fixed-fixed model showed larger $a_{rotate,inflect}$ than the fixed-pinned model.

3.4.3 Comparison with printed models

For comparison with the FE models, a pinned-pinned model, a pinned-fixed model, a fixed-pinned model, and a fixed-fixed model were printed by the PolyJet process using RGD8630-DM and FLEX9895-DM material. A geometric condition of *r15-a20-t0.9* was used for the printing of all models. In the printed part, the joints where the beam and the rotational part are connected by pin are implemented using water-soluble support material. When the rotational part and the beams are different materials, they are fabricated at once without any bonding process through multi-material printing.

Figure 3.24 (a) - (d) show the beam deflection of the pinned-pinned, pinned-fixed, fixed-pinned, and fixed-fixed models as their rotational angles increase. Comparing this with Figure 3.14-3.17, the shapes of the beam deflection shown in the FE model agreed with those of printed model. In addition, as shown in Figure 3.25 (a) and (b), pinned-pinned and pinned-fixed models have been shown to have bi-stability, as the beams are at rest when the external rotational load is removed with the inner rotational part rotated. The angles of the second stable state in printed models were 1.73 and 1.59 (rad), respectively, and the error of those in FE results (1.74 and 1.61) were within 1.26%. As shown in Figure 3.26 (a) and (b), the fixed-fixed model and the fixed-pinned model returned to their original stable state when the load is removed after turning the inner rotational part, confirming that it does not have bi-stability.

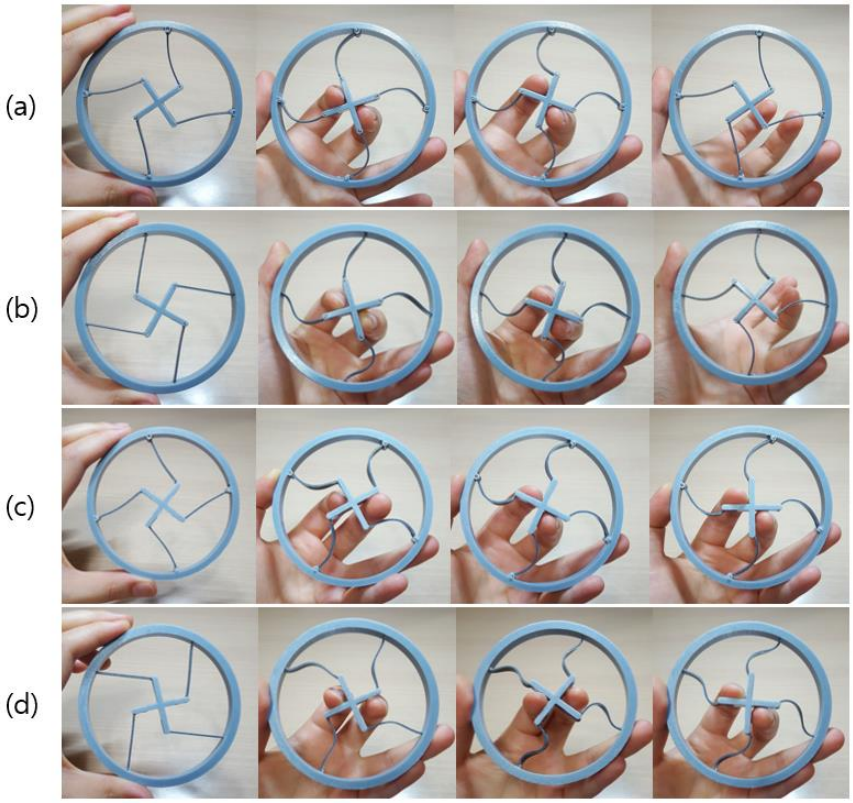

Figure 3.24 Beam deflections of (a) the pinned-pinned model. (b) the pinned-fixed model. (c) the fixed-pinned model. (d) the fixed-fixed model.

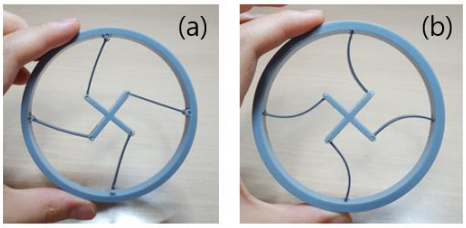

Figure 3.25 Second stable states of (a) the pinned-pinned model. (b) the pinned-fixed model.

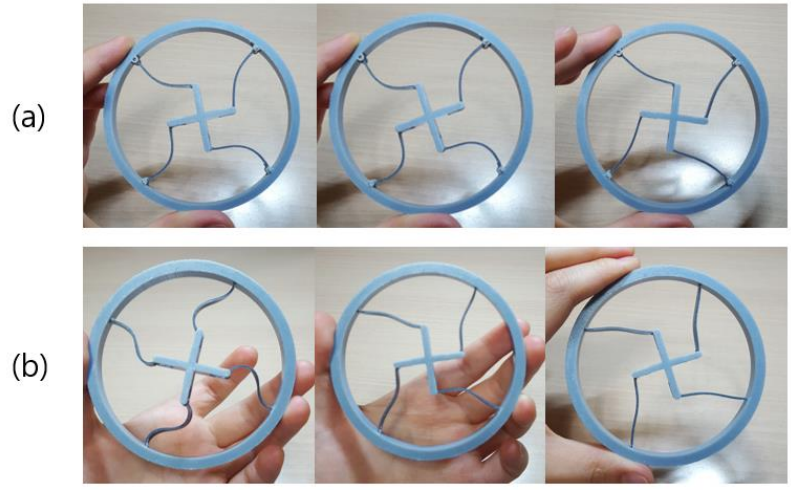

Figure 3.26 Shape recovery effect of (a) the fixed-pinned model. (b) the fixed-fixed model.

4. Design and FE simulation of the 4D rotational model

In the previous section, the properties of the rotatable models with four different beam connection types and the effect of the variables of geometry and material properties on their behavior and the strain energy have been examined. In this section, the results of the previous section is used to design a 4D printed part that has bi-stability at room temperature, but not at high temperatures. This model can be fixed in the second stable state at room temperature but restores its original stable state as the ambient temperature increases. This can be seen as a 4D printing that has rotational motion in response to a thermal stimulus, so the newly designed model is called the 4D rotational model. To see if the designed model has the intended function in the thermal stimulus, a thermal-displacement coupled FE simulation was conducted. Then the result was compared to the printed model for verification. The laboratory of Nanophotonics & Metamaterials, UNIST, conducted the DMA measurement of the material properties and the shape memory force, and suggested the initial idea and design of the 4D rotational model.

4.1 Design of the model

4.1.1 Design strategy for the 4D rotational model

A 4D rotational model which has bi-stability at room temperature and then loses this function at increased temperature should have the following characteristics:

1. The strain energy graph of the 4D rotational model at room temperature should have two minimum points. To increase the possibility of having bi-stability, the strain energy barrier between two stable positions must be maximized.

2. As the temperature increases, the energy barrier should be eliminated or minimized. At least, the energy barrier must be small enough to be overcome by the shape memory force of the SMP material.

In order to satisfy these two conflicting requirements, I noted the elastic moduli of the rigid material (RGD8530-DM) E_{rigid} and the rubbery material (FLEX9895-DM) E_{rubber}. The ratio of

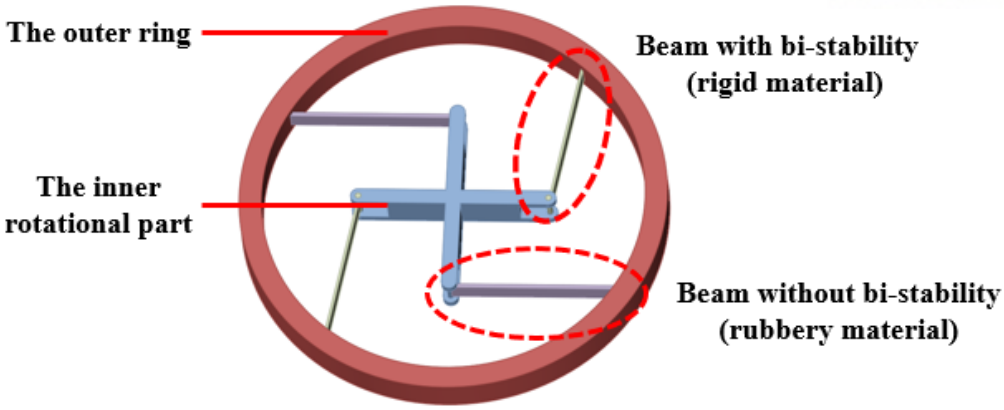

Figure 4.1 Structure of the 4D rotational model.

E_{rubber} to E_{rigid} is higher at T=70℃ than at T=20℃. Accordingly, I assumed that if a bi-stable beam with the rigid material and a non-bi-stable beam with the rubbery material are alternately arranged in a rotatable model, the whole model will have bi-stability at room temperature since the effect of the rigid beam will be larger. However, when the temperature is increased, the effect of the rubbery beam would grow, causing the whole part to lose bi-stability.

In a similar way to other rotatable models, the 4D rotational model consists of the fixed outer ring, the inner rotational part with a cross-shape, and four beams connecting them, as shown in Figure 4.1. The difference is that the four beam parts are alternately arranged with two rigid beams and two rubbery beams. The detailed geometries of the model not including the connection angles, the radius of the inner rotational part or the beam thicknesses are the same as the rotatable part in Figure 3.3.

4.1.2 Design of beams in the 4D rotational model

As shown in Figure 4.2, the process of designing the beam part of the 4D rotational model was as follows. First, a list of possible combinations of geometric parameters of the rigid beam and the rubbery beam was made. Second, the strain energy at room temperature and at high temperature were respectively estimated for every combination. Third, from the estimation result with the condition of room temperature, models with bi-stability, which had two local minima of the strain energy curve at room temperature, were selected. Fourth, from estimation result with condition of high temperature, models which had only one local minimum or the energy barrier small enough to be overcome by shape memory force were chosen. Finally, the combinations included in both sets of selected models were considered as candidates for the 4D rotational model.

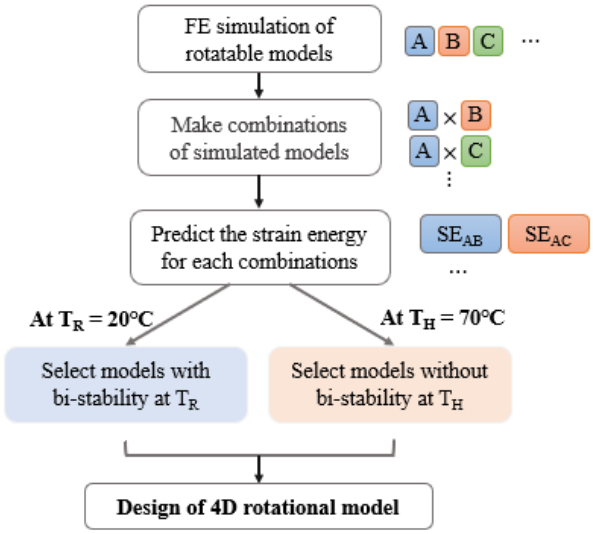

Figure 4.2 The process of designing the 4D rotational model.

Based on the strain energy results in Chapter 3, the pinned-pinned and the pinned-fixed connections were considered for rigid beams, and the fixed-fixed and the fixed-pinned connections were considered for rubbery beams. The method of combination of models is shown in Figure 4.3. First, the radius of the inner rotational part has two options of 15mm and 20mm, which is common in rigid and rubbery beams. Next, the connection types of rigid beams can be selected between the pinned-pinned connection and the pinned-fixed connection. Similarly, the possible connection types of the rubbery beam are the fixed-pinned connection and the fixed-fixed connection. The options for geometric variables are two connection angles of 0° and 20° and two beam thicknesses of 0.5mm and 0.9mm. By combining all of them, the strain energy prediction results for a total of 128 combinations were obtained.

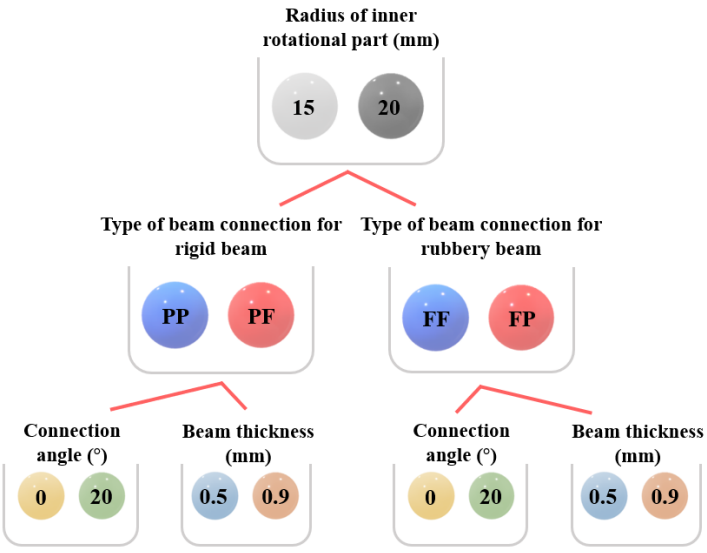

Figure 4.3 Element for combination in design of the 4D rotational model.

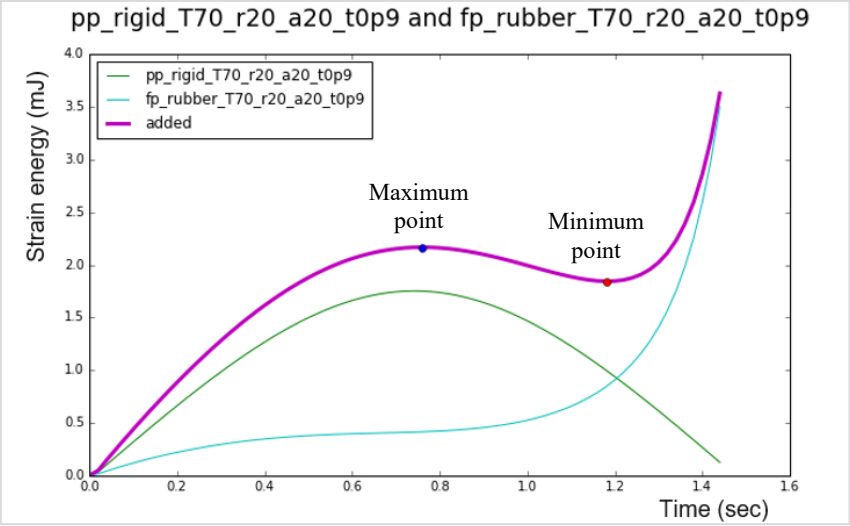

Figure 4.4 The example of estimated strain energy curve.

To predict the strain energy of models at room temperature and high temperature, I assume that the strain energy of the whole part is equal to the sum of the strain energy of each beam used. Therefore, the strain energy of the 4D rotational part (SE_{4D}) with combinations of the rigid beam in geometric condition A and rubbery beam in geometric condition B is assumed to be:

$$SE_{4D} = \frac{1}{2}SE_{rigid,A} + \frac{1}{2}SE_{rubbery,B}$$

Where $SE_{rigid,A}$ and $SE_{rubbery,B}$ are the strain energies of the rigid beam in condition A and that of the rubbery beam in condition B, respectively. The strain energies of rigid beam and rubbery beam were obtained from the FE simulation results in Section 3.4.2. Figure 4.4 shows an example of estimated strain energy curve, using strain energy results of *pp-rigid-T70-r20-a20-t0.9* model and *fp-rubber-T70-r20-a20-t0.9* model.

The predicted strain energy results at T=20℃ and T=70℃ are shown in Appendix. At T=20℃, the strain energy curves obtained from 66 in 128 combinations of models have two local minima. Although there is no model with only one minimum point at T=70℃ among the models, I still considered the possibility of shape recovery motion due to shape memory force F_{SM} in SMP. If F_{SM} is equal to or greater than the barrier force, F_B, the shape recovery motion will occur.

While F_{SM} is generated in both rigid and rubbery beams, F_{SM} in the rigid beam is considered to be negligible because it is canceled by force from the residual stress in the beam. Therefore, only F_{SM} in the rubbery beam was considered in this simulation. F_{SM} of the rubbery beam was calculated based on the result of the DMA measurement, by multiplying the geometrical, tangential and thickness factor, suggested by the laboratory of Nanophotonics & Metamaterials, UNIST, as described in the Appendix. The shape memory moment M_{SM} is calculated by multiplying F_{SM} to

r_{in}. The barrier moment M_B is the maximum slope of the points between the local maximum point and the second stable point of the predicted strain energy graph. Among the 66 models which have bi-stability at T=20℃, 32 models have M_{SM} larger than M_B. Table 4.1 shows the list of 10 combinations with the highest energy barrier at T=20℃. The list of all models is available in Appendix.

Among the candidates for the 4D rotational model, the combination of *pf-r20-a20-t0.5* model and *ff-r20-a20-t0.5* model was predicted to have the highest $SE_{barrier}$ at T=20℃ than the other combinations. Therefore, this model was expected to reliably provide the desired motion in the 4D rotational model, even with considering errors in simulation. This model will be referred to from now on as the 4D rotational model below.

Table 4.1 The list of 10 combinations with the highest $SE_{barrier}$ at T=20℃

Model used to predict SE in the rigid beam	Model used to predict SE in the rubbery beam	$SE_{barrier}$ at T=20℃ (mJ)	$SE_{barrier}$ at T=70℃ (mJ)	M_B (N·mm)	M_{SM} (N·mm)
pf-rigid-r20-a20-t0p5	*ff-rubber-r20-a20-t0p5*	18.366	0.179	0.359	0.273
pf-rigid-r20-a20-t0p5	*fp-rubber-r20-a20-t0p5*	17.712	0.158	0.303	0.273
pf-rigid-r20-a0-t0p9	*ff-rubber-r20-a20-t0p9*	17.469	0.136	0.566	0.466
pf-rigid-r20-a20-t0p5	*fp-rubber-r20-a0-t0p9*	16.931	0.147	0.283	0.314
pf-rigid-r20-a0-t0p9	*fp-rubber-r20-a20-t0p9*	14.826	0.069	0.288	0.466
pp-rigid-r15-a20-t0p9	*ff-rubber-r15-a20-t0p9*	14.056	0.058	0.193	0.362
pp-rigid-r15-a20-t0p5	*ff-rubber-r15-a0-t0p5*	13.012	0.102	0.138	0.154
pp-rigid-r20-a20-t0p5	*ff-rubber-r20-a0-t0p9*	11.808	0.086	0.225	0.314
pp-rigid-r15-a20-t0p9	*fp-rubber-r15-a20-t0p9*	11.41	0.019	0.078	0.362
pf-rigid-r20-a20-t0p5	*ff-rubber-r20-a0-t0p9*	10.275	0.072	0.212	0.314

4.2 FE simulation of the 4D rotational model

To identify the dynamic behavior and the strain energy change of the 4D rotational model, FE simulation was conducted using the same software as the one used in Chapter 3. The settings for FE modeling in the simulation process were similar to those presented in Section 3.3. However, the settings for the temperature-dependent material properties, the element types, the step settings, and the load condition for the shape memory force in this section is different from the previous section.

Material properties of the rigid material (RGD8530-DM) and rubbery material (FLEX9895-DM) were assumed to be isotropic and elastic, and the material arrangement was assumed to be homogeneous. Unlike the material setting used in Section 3.3.3, the temperature-dependent elastic modulus data measured by DMA were directly imported into the FEA software. Figure 4.5 is a graph showing elastic modulus-temperature data. the conductivity and specific heat of each material were input for temperature-displacement coupled analysis as well. For the rigid material and the rubbery material, the conductivities were assumed to be 2.376×10^2W/mm·℃ and 2.370×10^2W/mm·℃ [50], and specific heat of both material were assumed to be 2×10^9mJ/tonne·℃ [51], respectively. In this simulation, however, the thermal properties of materials did not directly affect the simulation results, since the temperature changes were given directly to the part, not by heat transfer.

The settings for mesh generation are the same as those used in Section 3.3.2, other than the use of element types for temperature-displacement coupled analysis. The inner rotational part and the outer ring are meshed with C3D4T element with grid sizes of 1.5mm and 4.5mm respectively. Beams are meshed using C3D8T elements with a grid size of 0.3mm. Table 4.2 shows the generated mesh information.

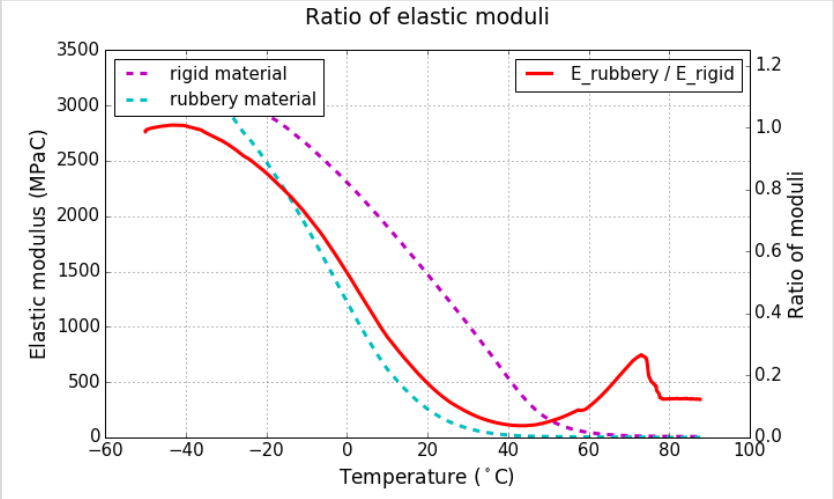

Figure 4.5 Ratio of elastic moduli of the rubbery material to the rigid material.

Table 4.2 The number of nodes and elements for a beam part

Beam type	Rigid beam	Rubbery beam
# of elements	2990	3990
# of nodes	4371	2444

The constraint settings for the 4D rotational model are also similar to those described in Section 3.3.4. The inner rotational part and the outer ring of the 4D rotational model are set as rigid bodies with reference points of RP1 and RP2, respectively. For the pinned connections, reference points are created at the center of each pin. These points are designated as the master points of the beam type MPC constraint with slave surfaces of the cylindrical part at the beam ends. Besides, they are set as pins in the rigid body option of inner rotational part and the outer ring. For the fixed connections, tie constraints are used. The master surfaces are designated to the surfaces of the inner rotational part and the outer ring, which are the rigid bodies, and the surfaces of the beams are set as slave surfaces in the tie constraint settings.

The simulation processes for the 4D rotational model are set with five steps. The first step (initial step) is for fixing the outer ring and setting the temperature to 25℃, which is applied throughout the analysis. The second step (Step 1) is for determining the trajectory of the beam deflection in the pinned-pinned connection and the fixed-pinned connection. The third step (Step 2) is for rotating the inner rotational part to the second stable state. At the fourth step (Step 3), the inner rotational part is released to rotate to the second stable state. The last step (Step 4) is the coupled temp-displacement step that enables the implementation of the shape-shifting effect caused by the temperature increase to 75℃. The F_{SM} is applied in terms of moments on the inner rotational part throughout all steps.

Here, the temperatures of 25℃ and 75℃ are used, instead of 20℃ and 70℃, since the DMA measurement of the shape memory force was conducted from 25℃ to 75℃. It is assumed that the temperature difference of 5℃ does not result in significant change in the result.

The specific settings of each step are shown in Table 4.3. In the initial step, RP2 is encastre so that the outer ring is fixed throughout the simulation. Plus, the ambient temperature of 25℃ is defined in setting of the predefined field. In Step 1, the moment of 0.01N·mm is applied to the reference point of the pinned-pinned connection (RP3-4) for 0.01 second. In Step 2, the reference point of the inner rotational part (RP1) is rotated at a velocity of 1rad/sec until the model reaches the second stable state. The duration time of Step 2 is approximated by the time of minimum point in the strain energy graph at 20℃ from Section 4.1.2. In Step 3, the angular velocity constraint on RP1 is inactivated for 0.1 seconds. This is for the free rotation of the inner rotational part to make sure the part moves to the second stable point where it has the lowest potential energy. In Step 4,

the temperature is linearly increased from 25°C to 75°C for 1.0 second and maintained for an additional second.

In principle, M_{SM} should be given as a temperature-dependent moment. However, since the simulation tool ABAQUS does not have function like that, the amplitude is made to vary the moment with respect to the time corresponding to the temperature setting. M_{SM} is applied to RP1 from Step 1 and continued to the end of Step 4. Until Step 2, M_{SM} does not work because RP1 is constrained to a boundary condition that defines angular velocity. It works from Step 3, and it is set to the increase nonlinearly with increasing temperature in Step 4.

Table 4.3 Step settings for the 4D rotational models

Step Setting					
	Initial step	**Step 1**	**Step 2**	**Step 3**	**Step 4**
BC1 : Fix RP2	Created	Continued	Continued	Continued	Continued
Predefined field: T=25°C	Created	Computed	Computed	Computed	Computed
Load case 1: M_{SM} applied at RP1	-	Created z-direction	Continued	Continued	Continued
Load case 2: Rotate pinned beam at 0.01N·mm	-	Created z-direction	Removed	Removed	Removed
BC2 : Rotate RP1 in 0.01rad/sec	-	-	Created -z-direction	Removed	Removed
BC3 : Temperature linearly increased to 75°C	-	-	-	-	Created
Duration times (sec)					
	-	0.01	1.175	0.1	2

4.3 Result and analysis

4.3.1 Dynamic behavior

Figure 4.6 shows the motion of the 4D rotational model. The beam deflections have shape like a mode-1 buckling, similar to that described in Section 3.4.1. The model is rotated to approach the stable state in Step 2 and reaches the stable state in Step 3. At this point, F_B and F_{SM} are in balance, so the model does not move.

As the temperature (T) rises in Step 4, the inner rotational part temporarily rotates in the -z-direction. This phenomenon occurs until $T \approx 44.6$℃. This is probably due to a change in the elastic modulus gap between the two materials as the temperature changes over time. As shown in Figure 4.5, the curve of the ratio of the two moduli in the materials decreases as the temperature decreases to about 44.6℃, then increases from about 62℃ to go beyond the value of 25℃. In temperatures lower than 44.6℃, the influence of F_B in the rigid beam is gradually increased as compared with the recovery force of the rubbery beam. Thus, the part rotates in the direction that the rigid beam is aimed at.

After 44.1℃, the direction of rotation changes as the influence of the rubbery beam gradually increases and F_{SM} increases. The inner rotational part slowly rotates until the temperature is about 74.7℃. After those points, the model rotates instantaneously to restore the original shape, in a similar way to the snap-through phenomenon. The temperature then rises to 75℃, but the parts keep their original shape. Thus, it is identified that the designed 4D rotational models are able to perform the intended function of shape recovery according to the temperature change.

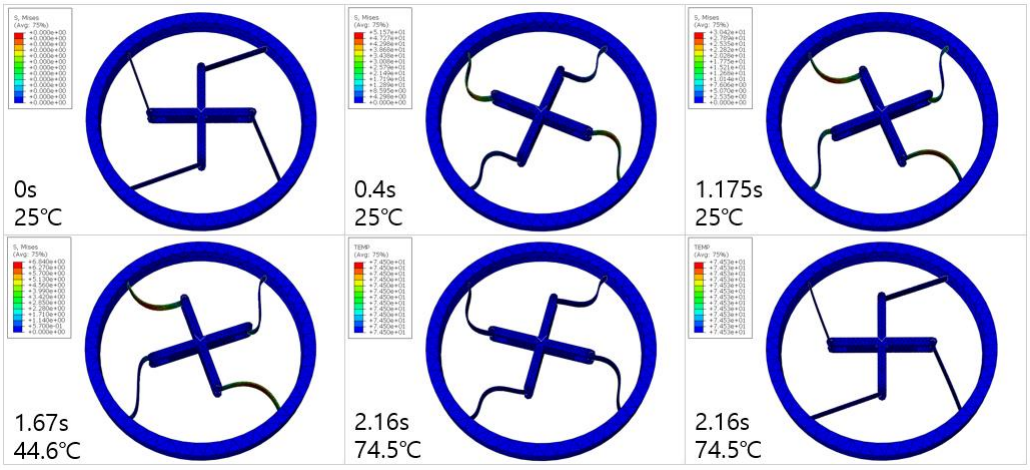

Figure 4.6 Motion in the 4D rotational model.

4.3.2 Strain energy

Figure 4.7 shows the strain energy to time curves from the result of FE simulation. This graph can be divided into two parts: one is where the inner rotational part rotates to the second stable point ($a_{rotate,stable2}$) in room temperature (T=25℃), and the other is where it returns to the original stable state where the strain energy decreases as T increases. Comparing the strain energy curve in section A to the estimated strain energy curve in Figure 4.8, the curves show similar form. The strain energy level in Figure 4.7 is lower than that of Figure 4.8, since the temperature was 25℃ in the former and 20℃ in the latter.

The highlighted part of section A is where the slope of the energy curve becomes zero as the part enters the second stable state. In section B, the graph has a decreasing shape because the elastic modulus of the whole material decreases as the temperature increases. The strain energy decreases sharply at 2.31 seconds in the fixed-pinned 4D rotational model. This point is where the inner rotational part returns quickly to the original stable state in a snap-through motion. After this point, the energy remains at zero because the model is already in equilibrium.

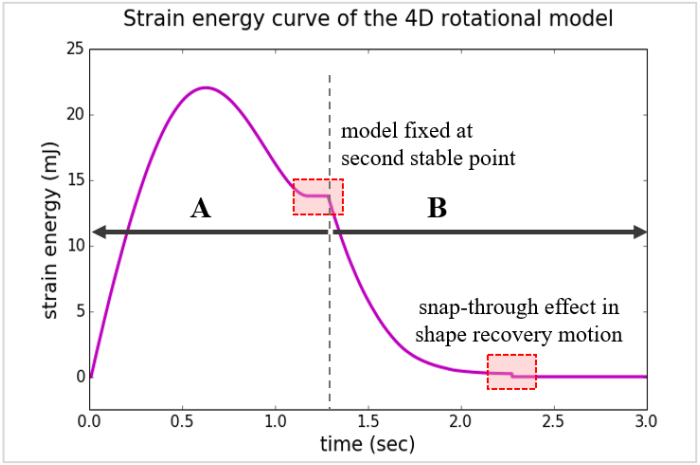

Figure 4.7 The strain energy curve of the 4D rotational model from FE simulation.

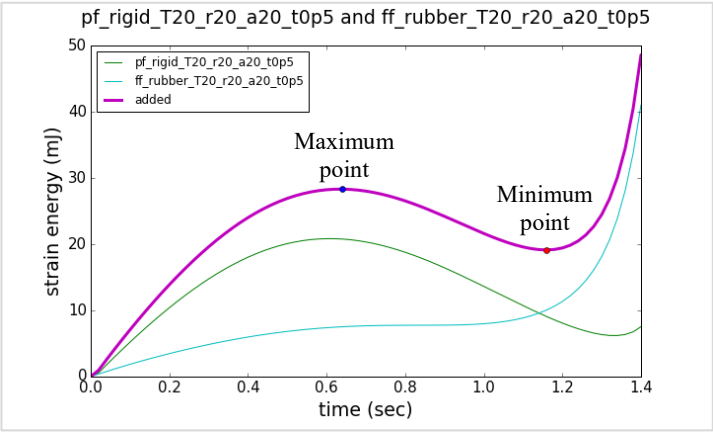

Figure 4.8 The estimated strain energy curve of the 4D rotational model.

4.3.3 Comparison with printed models and discussion

To verify that the designed model behaves the same as actual printed model, we printed the 4D rotational model with a PolyJet printer, as shown in Figure 4.9. Each model was rotated from room temperature to the second stable state. It is observed that rotational angle at the stable state is about 1.15 (rad), so that of the FE model (1.175) have error of about 2.2%.

The parts were then emerged in the water of 75℃. Then, it was observed that the rotation of the part was made after about 1.7s. The difference between the FE simulation and the rotation time is due to the difference in the speed of the temperature change. In the simulation, the temperature was linearly changed in order to observe the energy change due to the temperature change. However, in practice, the part is hydrated, thus the temperature of the model has nonlinear change due to the ambient temperature.

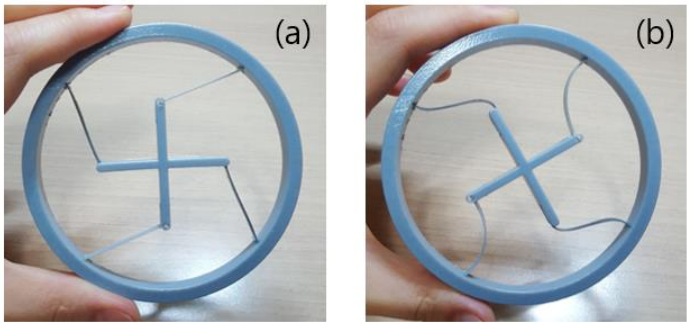

Figure 4.9 (a) the printed 4D rotational model. (b) second stable state of the 4D rotational model.

5. Conclusion

4D printing is the production of parts, which deform their shape for reaction to external stimuli, using 3D printing and smart materials. This enables the implementation of an active system that responds to stimulation without the use of sensors or actuators while allowing high design freedom that is not possible using conventional production methods. In the design of 4D printing, mathematical modeling is essential to predict the deformed shape of models and the effect of variables. This study uses computer simulation using FEM to design a multi-stable 4D rotational model which shifts its shape in response to thermal stimuli

In order to do that, firstly I analyzed models made of sub-component parts. The effect of variables on the strain energy of the rotatable models with bi-stability was investigated using FE simulation. In this process, the procedure of FE modeling with nonlinearity in material property and geometry was demonstrated. To increase convergence and reduce the computation time of simulation, contact conditions of the models were simplified, and the trajectories of beam deflection were pre-determined. The FE simulation results showed the effect of the parameters in material, model geometry, and temperature on the strain energy curve.

Using the strain energy graphs obtained from the FE simulation, a 4D rotational model was designed. This model can be fixed at the second stable position at low temperature, but it recovers the initially printed shape when heated. It has two types of beams which are alternately arranged. One has bi-stability and relatively high stiffness, and the other has recovery force and lower stiffness. The strain energy curves of all possible combinations of those two beam types were estimated for the 4D rotational models. Then, candidate models were selected considering the bi-stability in two temperature conditions inferred from the estimation data. For the newly designed model, FE coupled simulation including temperature-dependent shape memory force and mechanical properties was conducted. The FE result of strain energy showed good agreement with the estimation in the design process.

As shown in Figure 5.1, this study can be developed to the optimal design of the rotatable 4D printing part with multi-stability, which involves the accurate program of rotational motion in both space and time domains. The statistical analysis on the rotatable models provides the trend that how parameters affect the positions and the strain energies of stable states. The next step is to investigate the exact relationship of each parameter. In the end, the framework for the inverse calculation of the variables should be built, when the desired final deformed shape is given. The 4D rotational model designed through these processes can hold positions of two stable states and rotate in response to ambient stimuli without power input. The positions of stable states and the timescale of rotational

motion are programmable by adjusting model geometries. Consequently, many applications including active thermal switch and smart valve may benefit from it.

The data for the material properties used in this study was limited to the temperature-dependent elastic modulus, although the printed model has viscoelasticity which is an essential factor in the shape memory effect. In addition, in the experiment, the thermal stimulus was given via the heat transfer from the ambient environment. These factors were not considered in the simulation process of this thesis. I suggest that the difference between the FE model and the experiment are caused by these viewpoints. If the heat transfer and the viscoelastic material properties of SMP can be implemented in FE simulation through future research, the separate calculation of the shape memory force will not be necessary, and it will be possible to observe the delay in shape recovery motion due to temperature imbalance on the model.

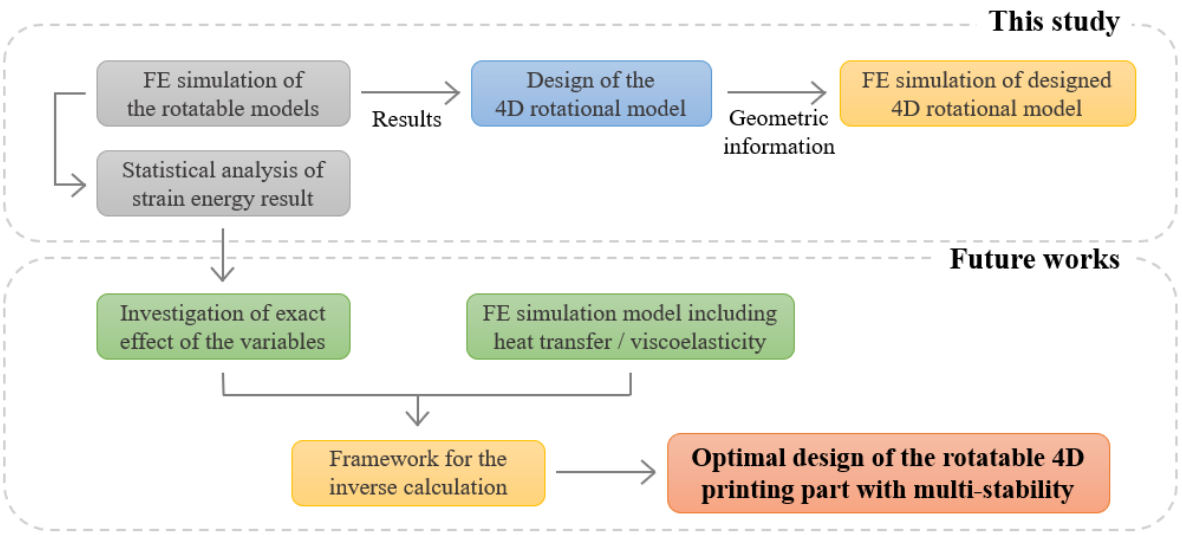

Figure 5.1 Steps for optimal design of the rotatable 4D printing part with multi-stability

Reference

1. Wohlers, T., et al., *Wohlers Report 2018*. 2018, Wohlers Associates.
2. Tibbits, S. *The emergence of "4D printing"*. in *TED conference*. 2013.
3. Sydney Gladman, A., et al., *Biomimetic 4D printing.* Nature Materials, 2016. **15**: p. 413.
4. Momeni, F., et al., *A review of 4D printing.* Materials & Design, 2017. **122**: p. 42-79.
5. Zarek, M., et al., *4D Printing of Shape Memory-Based Personalized Endoluminal Medical Devices.* Macromol Rapid Commun, 2017. **38**(2).
6. Mao, S., et al. *Locomotion and gait analysis of multi-limb soft robots driven by smart actuators*. in *2016 IEEE/RSJ International Conference on Intelligent Robots and Systems (IROS)*. 2016.
7. Zhang, Q., K. Zhang, and G. Hu, *Smart three-dimensional lightweight structure triggered from a thin composite sheet via 3D printing technique.* Sci Rep, 2016. **6**: p. 22431.
8. Čolić-Damjanovic, V. and I. Gadjanski. *Potentials of fablabs for biomimetic architectural research*. in *2016 International Conference Multidisciplinary Engineering Design Optimization (MEDO)*. 2016.
9. Khademhosseini, A. and R. Langer, *A decade of progress in tissue engineering.* Nature Protocols, 2016. **11**: p. 1775.
10. Mao, Y., et al., *3D Printed Reversible Shape Changing Components with Stimuli Responsive Materials.* Scientific Reports, 2016. **6**: p. 24761.
11. Raviv, D., et al., *Active Printed Materials for Complex Self-Evolving Deformations.* Scientific Reports, 2014. **4**: p. 7422.
12. Zhou, Y., et al., *From 3D to 4D printing: approaches and typical applications.* Journal of Mechanical Science and Technology, 2015. **29**(10): p. 4281-4288.
13. Chen, Z., et al., *Nonlinear geometric effects in mechanical bistable morphing structures.* Phys Rev Lett, 2012. **109**(11): p. 114302.
14. Bodaghi, M., A.R. Damanpack, and W.H. Liao, *Self-expanding/shrinking structures by 4D printing.* Smart Materials and Structures, 2016. **25**(10).
15. Leist, S.K. and J. Zhou, *Current status of 4D printing technology and the potential of light-reactive smart materials as 4D printable materials.* Virtual and Physical Prototyping, 2016. **11**(4): p. 249-262.
16. Vaupotic, B., et al., *Use of PolyJet technology in manufacture of new product.* 2006. **18**(1-2): p. 319-322.
17. Stratasys. *What is PolyJet Technology?* ; Available from: https://www.stratasys.com/polyjet-technology.
18. Rohrbeck, T. *What is PolyJet 3D Printing Technology?* 2017; Available from: https://www.gsc-3d.com/articles/2017/11/what-polyjet-3d-printing-technology.
19. Lipson, H. and J. Hiller, *Design and analysis of digital materials for physical 3D voxel printing.* Rapid Prototyping Journal, 2009. **15**(2): p. 137-149.
20. Tibbits, S., *4D Printing: Multi-Material Shape Change.* Architectural Design, 2014. **84**(1): p. 116-121.
21. Jamal, M., et al., *Bio-Origami Hydrogel Scaffolds Composed of Photocrosslinked PEG Bilayers.* Advanced Healthcare Materials, 2014. **2**(8): p. 1142-1150.

22. Mao, Y., et al., *Sequential Self-Folding Structures by 3D Printed Digital Shape Memory Polymers.* Scientific Reports, 2015. **5**: p. 13616.
23. Shin, D.-G., T.-H. Kim, and D.-E. Kim, *Review of 4D printing materials and their properties.* International Journal of Precision Engineering and Manufacturing-Green Technology, 2017. **4**(3): p. 349-357.
24. Kuksenok, O. and A.C. Balazs, *Stimuli-responsive behavior of composites integrating thermo-responsive gels with photo-responsive fibers.* Materials Horizons, 2016. **3**(1): p. 53-62.
25. Wu, J., et al., *Multi-shape active composites by 3D printing of digital shape memory polymers.* Scientific Reports, 2016. **6**: p. 24224.
26. Bakarich, S.E., et al., *4D Printing with Mechanically Robust, Thermally Actuating Hydrogels.* Macromol Rapid Commun, 2015. **36**(12): p. 1211-7.
27. Tibbits, S., et al., *4D Printing and universal transformation.* 2014.
28. Ge, Q., et al., *Multimaterial 4D Printing with Tailorable Shape Memory Polymers.* Scientific Reports, 2016. **6**: p. 31110.
29. Ge, Q., et al., *Active origami by 4D printing.* Smart Materials and Structures, 2014. **23**(9).
30. Mather, P.T., X. Luo, and I.A. Rousseau, *Shape Memory Polymer Research.* Annual Review of Materials Research, 2009. **39**(1): p. 445-471.
31. Ding, Z., et al., *Direct 4D printing via active composite materials.* Science Advances, 2017. **3**(4).
32. Nadgorny, M., et al., *Three-Dimensional Printing of pH-Responsive and Functional Polymers on an Affordable Desktop Printer.* ACS applied materials & interfaces, 2016. **8**(42): p. 28946.
33. Jinlian, H., et al., *A review of stimuli-responsive polymers for smart textile applications.* Smart Materials and Structures, 2012. **21**(5): p. 053001.
34. An, J., et al., *Design and 3D Printing of Scaffolds and Tissues.* Engineering, 2015. **1**(2): p. 261-268.
35. Carbonell, C. and A.B. Braunschweig, *Toward 4D Nanoprinting with Tip-Induced Organic Surface Reactions.* Acc Chem Res, 2017. **50**(2): p. 190-198.
36. Labonnote, N., et al., *Additive construction: State-of-the-art, challenges and opportunities.* Automation in Construction, 2016. **72**: p. 347-366.
37. Khoshnevis, B., *Automated construction by contour crafting—related robotics and information technologies.* Automation in Construction, 2004. **13**(1): p. 5-19.
38. Chen, G., Y. Gou, and L. Yang. *Research on Multistable Compliant Mechanisms: The State of the Art*. in *Proceedings of the 9th International Conference on Frontiers of Design and Manufacturing*. 2010.
39. Nazarov, Y.V. and J. Danon, *Advanced quantum mechanics: a practical guide*. 2013: Cambridge University Press.
40. Howell, L.L., *Compliant mechanisms*. 2001: John Wiley & Sons.
41. Oh, Y., *Synthesis of multistable equilibrium compliant mechanisms*. 2008, University of Michigan: [S.l.].
42. Timoshenko, S.P. and J.M. Gere, *Theory of elastic stability*. 1961, McGraw-Hill, New York.
43. Jin, Q., J.H. Lang, and A.H. Slocum, *A curved-beam bistable mechanism.* Journal of Microelectromechanical Systems, 2004. **13**(2): p. 137-146.
44. Tague, N.R., *The quality toolbox*. Vol. 600. 2005: ASQ Quality Press Milwaukee, WI.

45. Hibbett, Karlsson, and Sorensen, *ABAQUS/standard: User's Manual*. Vol. 1. 1998: Hibbitt, Karlsson & Sorensen.

46. Benzley, S.E., et al. *A comparison of all hexagonal and all tetrahedral finite element meshes for elastic and elasto-plastic analysis*. in *Proceedings, 4th international meshing roundtable*. 1995. Sandia National Laboratories Albuquerque, NM.

47. SAS Institute. *ANSYS Release 17.0 Tutorials*. 2016 June, 1, 2018]; Available from: https://www.sharcnet.ca/Software/Ansys/17.0/en-us/help/ans_mod/Hlp_G_MOD2_4.html.

48. Barclift, M.W. and C.B. Williams. *Examining variability in the mechanical properties of parts manufactured via polyjet direct 3D printing*. in *International Solid Freeform Fabrication Symposium*. 2012. University of Texas at Austin Austin, Texas.

49. Beer, F.P., E. Johnston, and J.T. Dewolf, *Mechanics of Materials. 6th*. 2012, McGraw-Hill. p. 572-701.

50. Kang, J.S., H. Wu, and Y. Hu, *Thermal Properties and Phonon Spectral Characterization of Synthetic Boron Phosphide for High Thermal Conductivity Applications.* Nano Letters, 2017. **17**(12): p. 7507-7514.

51. Kovacs, J.G., et al., *Evaluation of measured and calculated thermal parameters of a photopolymer.* International Communications in Heat and Mass Transfer, 2011. **38**(7): p. 863-867.

Appendix A: Strain energy result for the rotatable models

Table A.1 Strain energy result for the pinned-pinned models

Model name	$a_{rotate,stable2}$ (rad)	$SE_{barrier}$ (mJ)	Average *SE* until $a_{rotate,stable2}$
pp_rigid_T20_r15_a0_t0p5	2.3888	25.6453	15.3914
pp_rigid_T20_r15_a0_t0p9	2.3933	138.3983	83.2027
pp_rigid_T20_r15_a20_t0p5	1.7380	19.7792	12.2466
pp_rigid_T20_r15_a20_t0p9	1.7424	107.1693	59.5924
pp_rigid_T20_r20_a0_t0p5	2.1119	36.9170	21.7073
pp_rigid_T20_r20_a0_t0p9	2.1135	198.0754	116.5737
pp_rigid_T20_r20_a20_t0p5	1.4813	30.5812	18.7099
pp_rigid_T20_r20_a20_t0p9	1.4782	163.372	94.3013
pp_rigid_T70_r15_a0_t0p5	2.3260	0.2757	0.1734
pp_rigid_T70_r15_a0_t0p9	2.3836	1.4858	0.9007
pp_rigid_T70_r15_a20_t0p5	1.7325	0.2125	0.1329
pp_rigid_T70_r15_a20_t0p9	1.7456	1.1488	0.7122
pp_rigid_T70_r20_a0_t0p5	2.0740	0.3976	0.2415
pp_rigid_T70_r20_a0_t0p9	2.1092	2.1244	1.2592
pp_rigid_T70_r20_a20_t0p5	1.4865	0.3283	0.2020
pp_rigid_T70_r20_a20_t0p9	1.4794	1.7523	1.0666
pp_rubber_T20_r15_a0_t0p5	2.3900	4.4043	2.6495
pp_rubber_T20_r15_a0_t0p9	2.3864	23.7837	14.2643
pp_rubber_T20_r15_a20_t0p5	1.7502	3.4006	2.1117
pp_rubber_T20_r15_a20_t0p9	1.7436	18.4186	11.4897
pp_rubber_T20_r20_a0_t0p5	2.1146	6.3447	3.7577
pp_rubber_T20_r20_a0_t0p9	2.1163	34.0197	20.0549
pp_rubber_T20_r20_a20_t0p9	1.4776	28.0737	17.0729
pp_rubber_T70_r15_a0_t0p9	2.3840	0.3478	0.2115
pp_rubber_T70_r15_a20_t0p5	1.4878	0.0514	0.0378
pp_rubber_T70_r15_a20_t0p9	1.7400	0.2692	0.1680
pp_rubber_T70_r20_a0_t0p9	2.1081	0.4976	0.2961
pp_rubber_T70_r20_a20_t0p5	1.3577	0.0787	0.0533
pp_rubber_T70_r20_a20_t0p9	1.4789	0.4103	0.2511
pp_rubber_T70_r15_a0_t0p5	2.3820	0.0643	0.0392
pp_rubber_T70_r20_a0_t0p5	2.1080	0.0928	0.0552

Table A.2 Strain energy result for the pinned-fixed models

Model name	$a_{rotate,stable2}$ (rad)	$SE_{barrier}$ (mJ)	Average *SE* until $a_{rotate,stable2}$
pf_rigid_T20_r15_a0_t0p5	2.2292	30.7065	23.1909
pf_rigid_T20_r15_a0_t0p9	2.2915	166.7649	121.7164
pf_rigid_T20_r15_a20_t0p5	1.6051	22.6687	18.7070
pf_rigid_T20_r15_a20_t0p9	1.6149	128.9877	104.7156
pf_rigid_T20_r20_a0_t0p5	1.9166	40.3594	33.2714
pf_rigid_T20_r20_a0_t0p9	1.9400	224.2319	181.3015
pf_rigid_T20_r20_a20_t0p5	1.3302	29.3127	27.5050
pf_rigid_T20_r20_a20_t0p9	1.3353	228.8837	199.4331
pf_rigid_T70_r15_a0_t0p5	2.2687	0.3309	0.2433
pf_rigid_T70_r15_a0_t0p9	2.2847	1.7981	1.3209
pf_rigid_T70_r15_a20_t0p5	1.6154	0.2435	0.1997
pf_rigid_T70_r15_a20_t0p9	1.6044	1.3817	1.1271
pf_rigid_T70_r20_a0_t0p5	1.9172	0.4331	0.3565
pf_rigid_T70_r20_a0_t0p9	1.9208	2.4132	1.9665
pf_rigid_T70_r20_a20_t0p5	1.3291	0.3145	0.2955
pf_rigid_T70_r20_a20_t0p9	1.3377	1.8378	1.6873
pf_rubber_T20_r15_a0_t0p5	2.2573	5.3051	3.9347
pf_rubber_T20_r15_a0_t0p9	2.2963	28.6536	20.9922
pf_rubber_T20_r15_a20_t0p5	1.6071	3.8999	3.2078
pf_rubber_T20_r15_a20_t0p9	1.6109	22.1673	18.0499
pf_rubber_T20_r20_a0_t0p5	1.9191	6.9354	5.7123
pf_rubber_T20_r20_a0_t0p9	1.9482	38.4984	31.1031
pf_rubber_T20_r20_a20_t0p5	1.3335	5.0373	4.7199
pf_rubber_T20_r20_a20_t0p9	1.3216	29.6460	26.1318
pf_rubber_T70_r15_a0_t0p5	2.2087	0.0797	0.0604
pf_rubber_T70_r15_a0_t0p9	1.8939	0.4170	0.3747
pf_rubber_T70_r15_a20_t0p5	1.5697	0.0588	0.0496
pf_rubber_T70_r15_a20_t0p9	1.6175	0.3244	0.2639
pf_rubber_T70_r20_a0_t0p5	1.8806	0.1034	0.0868
pf_rubber_T70_r20_a0_t0p9	1.8200	0.6112	0.5233
pf_rubber_T70_r20_a20_t0p5	1.3105	0.0752	0.0715
pf_rubber_T70_r20_a20_t0p9	1.3317	0.4307	0.3964

Table A.3 Strain energy result for the fixed-fixed models

Model name	$a_{rotate,inflect}$ (rad)	$SE_{inflect}$ (mJ)	Average *SE* until $a_{rotate,inflect}$
ff_rigid_T20_r15_a0_t0p9	1.0522	304.2533	177.2507
ff_rigid_T20_r15_a20_t0p9	0.8549	300.7690	186.5034
ff_rigid_T20_r20_a0_t0p5	1.1691	105.5858	67.2507
ff_rigid_T20_r20_a0_t0p9	1.1654	565.2438	349.4992
ff_rigid_T20_r20_a20_t0p5	0.7847	90.8683	58.7087
ff_rigid_T20_r20_a20_t0p9	0.8515	512.6402	337.1226
ff_rigid_T70_r15_a0_t0p9	1.0522	3.2613	1.9000
ff_rigid_T70_r15_a20_t0p9	0.8549	3.2240	1.9992
ff_rigid_T70_r20_a0_t0p5	1.1691	1.1318	0.7209
ff_rigid_T70_r20_a0_t0p9	1.1654	6.0589	3.7463
ff_rigid_T70_r20_a20_t0p5	0.7720	0.9739	0.6393
ff_rigid_T70_r20_a20_t0p9	0.8515	5.4951	3.6137
ff_rubber_T20_r15_a0_t0p9	1.0522	52.2845	30.4597
ff_rubber_T20_r15_a20_t0p9	0.8549	51.6858	32.0497
ff_rubber_T20_r20_a0_t0p5	1.1691	18.1444	11.5567
ff_rubber_T20_r20_a0_t0p9	1.1654	97.1345	60.0598
ff_rubber_T20_r20_a20_t0p5	0.8300	15.5262	10.6213
ff_rubber_T20_r20_a20_t0p9	0.8515	88.0948	57.9329
ff_rubber_T70_r15_a0_t0p9	1.0522	0.7637	0.4449
ff_rubber_T70_r15_a20_t0p9	0.8549	0.7550	0.4682
ff_rubber_T70_r20_a0_t0p5	1.1691	0.2650	0.1688
ff_rubber_T70_r20_a0_t0p9	1.1654	1.4189	0.8773
ff_rubber_T70_r20_a20_t0p9	0.8515	1.2868	0.8462
ff_rigid_T20_r15_a20_t0p5	0.8672	54.1140	34.7015
ff_rigid_T70_r15_a0_t0p5	1.0175	0.6614	0.4446
ff_rigid_T70_r15_a20_t0p5	0.8675	0.5804	0.3730
ff_rubber_T20_r15_a0_t0p5	1.1300	10.5421	6.4242
ff_rubber_T20_r15_a20_t0p5	0.8675	9.3026	5.9706
ff_rubber_T70_r15_a0_t0p5	1.1175	0.1542	0.0952
ff_rubber_T70_r15_a20_t0p5	0.8475	0.1367	0.0911
ff_rubber_T70_r20_a20_t0p5	0.8275	0.2274	0.1550

Table A.4 Strain energy result for the fixed-pinned models

Model name	$a_{rotate,inflect}$ (rad)	$SE_{inflect}$ (mJ)	Average *SE* until $a_{rotate,inflect}$
fp_rigid_T20_r15_a0_t0p5	1.7840	76.3128	30.7715
fp_rigid_T20_r15_a20_t0p5	1.3570	64.4843	21.0885
fp_rigid_T20_r15_a20_t0p9	1.0982	157.2834	85.0225
fp_rigid_T20_r20_a0_t0p5	1.8298	173.2191	43.6101
fp_rigid_T20_r20_a0_t0p9	1.0036	199.1523	130.1871
fp_rigid_T20_r20_a20_t0p5	1.2009	76.1758	29.5599
fp_rigid_T70_r15_a0_t0p5	1.7855	0.8264	0.2822
fp_rigid_T70_r15_a0_t0p9	1.3485	1.9463	1.0663
fp_rigid_T70_r15_a20_t0p5	1.3607	0.7061	0.2287
fp_rigid_T70_r15_a20_t0p9	1.1037	1.7042	0.9154
fp_rigid_T70_r20_a0_t0p5	1.8207	1.7944	0.4628
fp_rigid_T70_r20_a0_t0p9	1.4420	3.2025	1.7295
fp_rigid_T70_r20_a20_t0p5	1.1983	0.8106	0.3167
fp_rubber_T20_r15_a0_t0p5	1.7867	13.1997	4.5017
fp_rubber_T20_r15_a0_t0p9	1.3464	31.1179	17.0679
fp_rubber_T20_r15_a20_t0p5	1.3606	11.2374	3.6435
fp_rubber_T20_r15_a20_t0p9	1.0979	27.0159	14.6067
fp_rubber_T20_r20_a0_t0p5	1.8207	28.5766	7.3886
fp_rubber_T20_r20_a0_t0p9	1.0036	34.2234	22.3720
fp_rubber_T20_r20_a20_t0p5	1.1994	13.0000	5.0677
fp_rubber_T70_r15_a0_t0p5	1.8618	0.2711	0.0802
fp_rubber_T70_r15_a0_t0p9	1.3370	0.4507	0.2492
fp_rubber_T70_r15_a20_t0p9	1.0970	0.3951	0.2142
fp_rubber_T70_r20_a0_t0p5	1.8002	0.4283	0.1125
fp_rubber_T70_r20_a0_t0p9	1.4480	0.7576	0.4064
fp_rubber_T70_r20_a20_t0p5	1.1830	0.1921	0.0771
fp_rigid_T20_r15_a0_t0p9	0.8579	122.3432	72.9523
fp_rigid_T20_r20_a20_t0p9	0.6660	161.2162	108.2767
fp_rigid_T70_r20_a20_t0p9	0.6601	1.7256	1.1553
fp_rubber_T20_r20_a20_t0p9	0.6616	27.6735	18.5388
fp_rubber_T70_r15_a20_t0p5	0.6275	0.0458	0.0298
fp_rubber_T70_r20_a20_t0p9	0.6619	0.4047	0.2718

Appendix B: Strain energy estimation result for the 4D rotational model

Table A.5 Strain energy estimation result for the 4D rotational models

Model used to predict SE in the rigid beam	Model used to predict SE in the rubbery beam	$SE_{barrier}$ at T=20°C (mJ)	$SE_{barrier}$ at T=70°C (mJ)	M_B (N·mm)	M_{SM} (N·mm)
pf_rigid_T70_r15_a0_t0p5	ff_rubber_T70_r15_a0_t0p5	9.9795	0.0772	0.1206	0.1542
pf_rigid_T70_r15_a0_t0p5	fp_rubber_T70_r15_a0_t0p5	9.7430	0.0603	0.0943	0.1542
pf_rigid_T70_r15_a20_t0p5	ff_rubber_T70_r15_a0_t0p9	3.0874	0.0052	0.0236	0.2630
pf_rigid_T70_r15_a20_t0p5	ff_rubber_T70_r15_a20_t0p5	9.3205	0.0724	0.1448	0.2121
pf_rigid_T70_r15_a20_t0p5	fp_rubber_T70_r15_a0_t0p9	4.6455	0.0192	0.0563	0.2630
pf_rigid_T70_r15_a20_t0p5	fp_rubber_T70_r15_a20_t0p5	8.3325	0.0645	0.1241	0.2121
pp_rigid_T70_r15_a0_t0p5	ff_rubber_T70_r15_a0_t0p5	1.3309	0.0052	0.0186	0.1542
pp_rigid_T70_r15_a0_t0p9	ff_rubber_T70_r15_a0_t0p9	6.1198	0.0091	0.0571	0.2630
pp_rigid_T70_r15_a0_t0p9	fp_rubber_T70_r15_a0_t0p9	7.6077	0.0052	0.0325	0.2630
pp_rigid_T70_r15_a20_t0p5	ff_rubber_T70_r15_a0_t0p5	13.0124	0.1022	0.1380	0.1542
pp_rigid_T70_r15_a20_t0p5	fp_rubber_T70_r15_a0_t0p5	10.2751	0.0878	0.1155	0.1542
pp_rigid_T70_r15_a20_t0p9	ff_rubber_T70_r15_a20_t0p9	14.0560	0.0579	0.1930	0.3617
pp_rigid_T70_r15_a20_t0p9	fp_rubber_T70_r15_a20_t0p9	11.4104	0.0186	0.0775	0.3617
pf_rigid_T70_r20_a0_t0p5	ff_rubber_T70_r20_a0_t0p9	8.3156	0.0570	0.1781	0.4183
pf_rigid_T70_r20_a0_t0p5	ff_rubber_T70_r20_a20_t0p5	2.5882	0.0178	0.0811	0.3646
pf_rigid_T70_r20_a0_t0p5	fp_rubber_T70_r20_a0_t0p9	4.8615	0.0227	0.0810	0.4183
pf_rigid_T70_r20_a0_t0p5	fp_rubber_T70_r20_a20_t0p5	1.8367	0.0012	0.0115	0.3646
pf_rigid_T70_r20_a0_t0p9	ff_rubber_T70_r20_a20_t0p9	17.4690	0.1358	0.5658	0.6217
pf_rigid_T70_r20_a0_t0p9	fp_rubber_T70_r20_a20_t0p9	14.8261	0.0690	0.2877	0.6217
pf_rigid_T70_r20_a20_t0p5	ff_rubber_T70_r20_a0_t0p9	10.2747	0.0722	0.2124	0.4183
pf_rigid_T70_r20_a20_t0p5	ff_rubber_T70_r20_a20_t0p5	18.3664	0.1794	0.3589	0.3646
pf_rigid_T70_r20_a20_t0p5	ff_rubber_T70_r20_a20_t0p9	9.2797	0.0803	0.3088	0.6217
pf_rigid_T70_r20_a20_t0p5	fp_rubber_T70_r20_a0_t0p9	16.9312	0.1471	0.2829	0.4183
pf_rigid_T70_r20_a20_t0p5	fp_rubber_T70_r20_a20_t0p5	17.7117	0.1576	0.3031	0.3646
pf_rigid_T70_r20_a20_t0p5	fp_rubber_T70_r20_a20_t0p9	5.9481	0.0410	0.1368	0.6217
pp_rigid_T70_r20_a0_t0p5	ff_rubber_T70_r20_a0_t0p5	8.4970	0.0791	0.1647	0.2453
pp_rigid_T70_r20_a0_t0p5	fp_rubber_T70_r20_a0_t0p5	7.0535	0.0459	0.0998	0.2453
pp_rigid_T70_r20_a20_t0p5	ff_rubber_T70_r20_a0_t0p9	11.8082	0.0855	0.2250	0.4183
pp_rigid_T70_r20_a20_t0p5	ff_rubber_T70_r20_a20_t0p5	7.4355	0.0664	0.1845	0.3646
pp_rigid_T70_r20_a20_t0p5	ff_rubber_T70_r20_a20_t0p9	1.8828	0.0127	0.0904	0.6217
pp_rigid_T70_r20_a20_t0p5	fp_rubber_T70_r20_a0_t0p9	9.7066	0.0647	0.1471	0.4183
pp_rigid_T70_r20_a20_t0p5	fp_rubber_T70_r20_a20_t0p5	6.4832	0.0397	0.1103	0.3646

Appendix C: Calculation of the shape memory force

Shape memory force of the rubbery beams in the 4D rotational model is calculated based on the DMA data. Following equation is the calculation of the shape memory force.

$$F_{SM} \sim F_{DMA} \times n_{beam} \times k_{geometry} \times k_{thickness} \times k_{tan}$$

where each factor of the equation is as follows:

1. $\boldsymbol{F_{SM}}$: shape memory force

2. $\boldsymbol{F_{DMA}}$: shape memory force data from DMA measurement

   The DMA measurement was conducted in the constrained-recovery condition, using TA Instruments Q800. The size of sample used in the measurement was 22.47 mm x 8 mm x 1 mm. The temperature was increased from 26℃ to 75℃ with a rate of 2℃ per minute. The measured F_{DMA} is shown in Figure A.1.

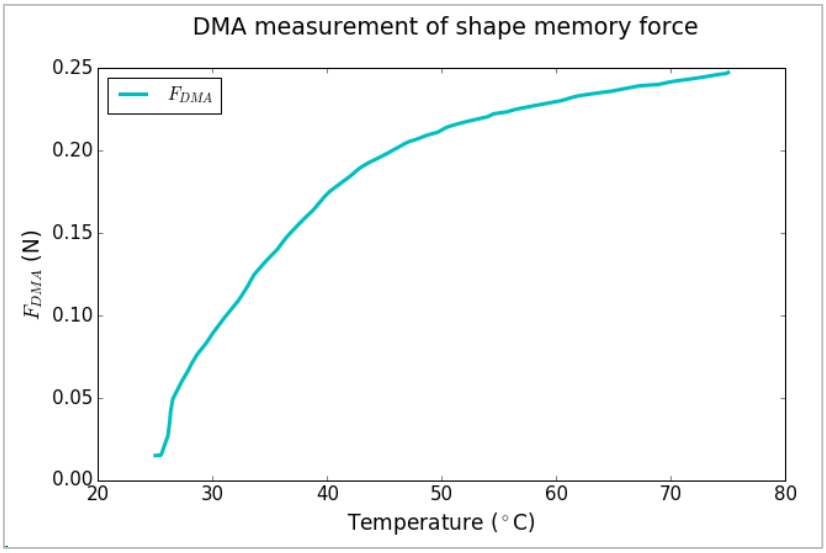

Figure A.1 DMA measurement of shape memory force

3. $\boldsymbol{n_{beam}}$: the number of the rubbery beams

4. $\boldsymbol{k_{geometry}}$: geometrical factor

   The geometrical factor is calculated due to the beam length. According to the beam theory, the bending force of a beam is inversely proportional to the square of the length of the beam. Therefore, the geometrical factor is obtained as follows:

$$k_{geometry} = \left(\frac{l_{DMA}}{l_{beam}}\right)^{-2}$$

where l_{DMA} is the length of the beam used in DMA measurement (22.47mm), and l_{beam} is the length of the rubbery beam in the 4D rotational model.

5. $K_{thickness}$: thickness-dependence factor

According to the beam theory, the bending force of a beam is proportional to the cube of the thickness of the beam. Therefore, the geometrical factor can be calculated as follows:

$$k_{thickness} = \left(\frac{t_{beam}}{t_{DMA}}\right)^3 = t_{ratio}^3$$

where t_{beam} is the thickness of the rubbery beam in the 4D rotational model, t_{DMA} is the thickness of the beam used in DMA measurement (1.0mm), and t_{ratio} is the ratio of two thickness values. For the more accurate value, following thickness-dependence factors are obtained from FE simulation results:

t_{beam}	0.4 mm	0.6 mm	0.8 mm	1.0 mm	1.2 mm
$k_{thickness}$	0.074	0.245	0.535	1	1.859

The equation of the cubic regression of these values is

$$k_{thickness} = \ 2.8646t_{ratio}^3 - 4.1054t_{ratio}^2 + 2.8415t_{ratio} - 0.5914$$

6. k_{tan}: Tangential force factor

Although the shape memory force is generated in every element in the rubbery beam, the shape memory force normal to the inner rotational part can affect the rotational recovery motion of the 4D rotational model. The following tangential force factors, that indicates the levels of contribution to the rotational moment, are obtained from FE simulation result.

t_{beam}	0.4 mm	0.6 mm	0.8 mm	1.0 mm	1.2 mm
k_{tan}	0.563	0.289	0.173	0.104	0.077

The equation of the cubic regression of these values is

$$k_{tan} = \ -1.2083t_{ratio}^3 - 3.8661t_{ratio}^2 - 4.2799t_{ratio} + 1.7322$$

Acknowledgements

First of all, I wish to express my gratitude to my advisor, Prof. Namhun Kim for his constant encouragement and guidance with wise advice. I was honored to be able to study under Prof. Kim, who has great insight and broad knowledge in mechanical and industrial engineering. I will never forget kindness and patience he showed in every work I have done. Also, I sincerely appreciate my thesis examining committee member, Prof. Young Chul Jeon and Prof. Sang Hoon Kang, for their practical advice and considerate encouragement. I want to extend my gratitude to Prof. Young Chul Jeon, who gave me a chance to participate in such good research.

I have learned a lot from the members of UNIST Computer Integrated Manufacturing (UCIM) lab. I would like to appreciate PhDs in UCIM lab, Dr. Eunju Park, Dr. JuYoun Gwon, and Dr. Moise Busogi, who gave me advice from their experience and insight. I am also grateful to the students in the PhD program, Sangho Ha, Jeongsik Kim, and Donghwan Song. They taught me the life of a graduate student and helped me a lot in completing my thesis. My colleagues, Hae Joon Choi and Moonyoung Lee stayed up many nights with me working together for graduation. Even if they are older than me, we became good friends, and I will miss them. I also enjoyed working together with Ga-hyung Kim, Tae Yang Choi, and Hae Kwon Jung. I wish good luck to their remaining days in UCIM lab. In addition, I would like to thank 3DAM members. Especially, Jae-boon Kim helped 3D printing the parts in this work.

I owe my heartful gratitude to my family. I feel lucky that I grew up in such a loving and trusted family. Mom and Dad always have trusted me in what I did and have been providing all sort of supports without hesitation. My brother is my best friend and also a supporter. I promise them that I will always try to remain a proud daughter and sister to my family.

Last but not least, I would like to say thank you to all those who did not mention it.